

1 **Impacts of orography and urbanization on extreme**
2 **precipitation event in Beijing during 2023**

3

4 Haobo Cui¹, Hongyong Yu¹, Xingshuo Zuo¹ and Guocan Wu^{1*}

5

6 ¹State Key Laboratory of Earth Surface Processes and Disaster Risk Reduction,
7 Faculty of Geographical Science, Beijing Normal University, Beijing, 100875 China

8

**Corresponding author: Guocan Wu*

E-mail address: gcwu@bnu.edu.cn

9 **Abstract**

10 The effects of urbanization and orographic uplift play significant roles in extreme
11 precipitation events, and therefore in water management. In this study, the main
12 impact factors in an extreme precipitation event that occurred during July 2023 in
13 Beijing were analyzed, using the Weather Research and Forecasting (WRF) model.
14 The results showed that the main cause of this precipitation event was the residual
15 forces of Typhoon Doksuri combined with water vapor transported from the
16 subtropical high. The orographic effect altered the spatial pattern of accumulated
17 precipitation throughout the simulation period by changing the local circulation, as the
18 accumulated precipitation in the southwestern mountainous regions increased by
19 229.4 mm (41.34%), and the precipitation in the plain areas decreased by 83.6 mm
20 (43.50%). The impact of the underlying urban surface led to accumulated
21 precipitation in the southwestern mountainous regions of Beijing decreasing by 88.1
22 mm (15.87%). Further analysis showed that orographic features caused the uplift of
23 air masses in the mountainous regions and prevented the low-pressure system from
24 propagating, leading to significant enhancement of the convective intensity over
25 Beijing and precipitation for a prolonged duration. The presence of urban surfaces
26 contributed to reductions in the latent heat flux and wind speed, resulting in decreased
27 energy transfer to the southwestern mountainous regions via easterly winds. This
28 reduction in energy suppressed convective activity and subsequently led to a decrease
29 in precipitation in these regions. As extreme precipitation events become more
30 frequent, the comprehensive research into such events may help with prevention and
31 the response to similar events in the future.

32 **Keywords:** WRF model; Precipitation simulation; orographic impacts; Urbanization;
33 Beijing area

34

35 **1. Introduction**

36 In the precipitation process, water vapor in the atmosphere condenses and falls to
37 the Earth's surface in the form of liquid or solid as a crucial component of the global
38 water cycle (Gimeno et al. 2010; Trenberth et al. 2003). Unlike other climatic
39 variables, precipitation is typically discontinuous in a given location and its temporal
40 distribution is uneven (Pendergrass and Knutti 2018; Wu et al. 2021). Extreme
41 precipitation events, characterized by high precipitation rates over short durations or
42 prolonged accumulated precipitation, often result in natural disasters such as floods
43 and landslides. These events can disrupt ecosystems, agricultural production, and
44 cause significant economic damage and loss of life (Ayat et al. 2022; Mahoney 2016;
45 Yu et al. 2024). Therefore, extreme precipitation has become a major focus of
46 research in weather and climate research (Dai et al. 2024; Li et al. 2024a; Sun et al.
47 2021; Zhang et al. 2022).

48 Orography is one of the most critical factors in land-air interaction, due to its
49 capacity to alter precipitation patterns through a variety of complex processes (Smith
50 2006). Mountains can modify the spatial distribution of precipitation by blocking and
51 uplifting air masses to alter the atmospheric properties at different elevations on both
52 the windward and leeward sides (Cornejo et al. 2024; Davolio et al. 2009; Lin et al.
53 2001; Wei et al. 2023). Meanwhile, orographic forcing can also influence the
54 temperature and humidity of the lower atmosphere, which alters the distribution of
55 convection by controlling the buoyancy of air masses to increase the moisture content
56 over the foothills, thereby promoting precipitation in these regions (Du et al. 2020;
57 Gao et al. 2021; Nicolas and Boos 2024; Xia and Zhang 2019; Yin et al. 2020). In
58 addition, the thermodynamic differences between mountainous areas and plains give
59 rise to local thermal circulations, which are among the physical processes that
60 influence the spatial distribution and diurnal variation of precipitation (Chen et al.
61 2014; He and Zhang 2010). The altitude used in the numeric model can affect the
62 regional water vapor flux, especially the channel of moisture in the lower and middle
63 troposphere (Saurral et al. 2015). Therefore, the influence of orography is particularly

64 significant for determining precipitation patterns in mountainous regions and
65 surrounding plains.

66 Due to human activities, altered land use patterns caused by urbanization are
67 another key factor that needs to be considered in precipitation events (Dou et al. 2015;
68 Huang et al. 2019; Niyogi et al. 2011). The emergence of urban areas has led to the
69 development of unique urban canopies and urban boundary layers, giving rise to the
70 urban heat island (UHI) effect, thereby causing convergence and upward lifting in the
71 lower atmosphere (Bornstein and Lin 2000; Hjelmfelt 1982). The UHI effect can
72 enhance boundary layer turbulence mixing by increasing the surface heat flux to
73 strengthen boundary layer instability and lead to precipitation (Holst et al. 2016; Nie
74 et al. 2017). This effect is especially significant for mesoscale and small-scale
75 circulations and convection (Dixon and Mote 2003; Oke 1982; Yin et al. 2020; Zhang
76 et al. 2017), which induces convective activity in urban and surrounding areas, and
77 changes in precipitation patterns (Fu et al. 2024; Li et al. 2011; Yang et al. 2017).
78 However, precipitation respond to urbanization varies under different degree of land
79 use change climatic backgrounds (Wang et al. 2015). The “urban rain island” effect
80 may be observed in some coastal cities with abundant moisture transport (Jauregui
81 and Romales 1996; Wang et al. 2018), whereas the depletion of moisture in the lower
82 atmosphere caused by urban activities may lead to the “urban dry island” effect in
83 relatively arid cities (Freitag et al. 2018; Wang and Gong 2010). Therefore, the
84 mechanisms that urbanization influences extreme precipitation events are complex,
85 necessitating further research to clarify the roles of cities in these events.

86 Beijing is located in the northwest of the North China Plain, where is the
87 transitional zone between the Taihang Mountains, Yanshan Mountains, and North
88 China Plain. It is an international metropolis with a population of over 10 million and
89 its surrounding areas have experienced rapid urbanization since the 1980s. In recent
90 years, Beijing and neighboring areas of Hebei and Tianjin have frequently
91 experienced high-intensity extreme precipitation events during the summer months
92 (Tewari et al. 2022; Yu et al. 2017; Zhang et al. 2013b; Zhong et al. 2015). Some

93 previous studies have provided evidence of increases in the frequency of extreme
94 precipitation events in large cities (Liang and Ding 2017), and Beijing is a
95 representative region for studying these events.

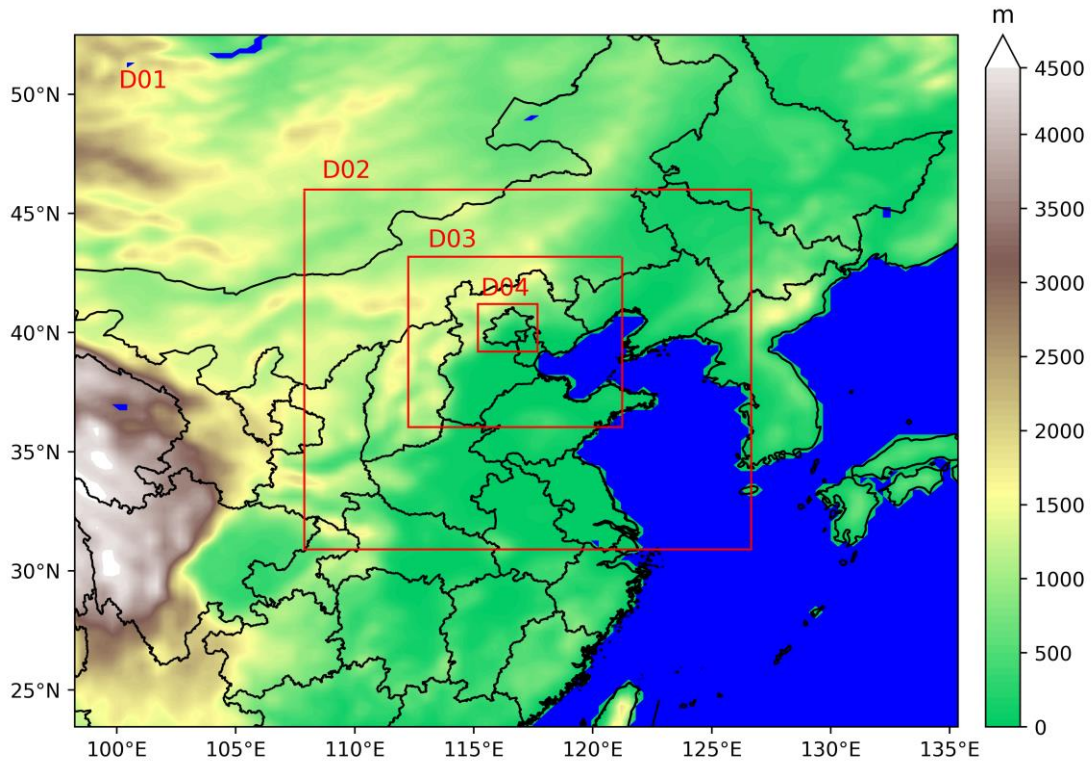
96 In this study, an extreme precipitation event that occurred in Beijing from July 29
97 to August 2, 2023 was analyzed, using the Weather Research and Forecasting model
98 (WRF). The accumulated precipitation distribution had a clear pattern, with higher
99 amounts in the southwestern mountainous areas and lower amounts in the
100 northeastern regions. Therefore, both the orographic effect and urban land use could
101 have potentially influences to the precipitation spatial pattern, which were assessed by
102 the comparisons of several experiment schemes. The causes of the event and the
103 related mechanisms were examined, by quantifying the effects of orography, land use,
104 and other factors on the precipitation event.

105

106 **2. Data and Methodology**

107 2.1. Study Area and Precipitation Event

108 The present study focused on the “23·7” precipitation event that occurred in
109 Beijing area (shown in region D04 in Figure 1) during July 2023. From July 29 to
110 August 2, 2023, a severe and prolonged heavy rainfall event affected Beijing and
111 neighboring areas of Tianjin and Hebei. This event was driven by the residual forces
112 of Typhoon Doksuri moving northward and the influence of Typhoon Khanun. The
113 average precipitation in the Beijing region exceeded 300 mm, where the most affected
114 areas, including Fangshan and Mentougou districts, recorded average accumulated
115 rainfall amounts greater than 500 mm (Li et al. 2024c). The rainstorm also triggered
116 severe flooding and urban waterlogging, resulting in significant damage to
117 infrastructure and property across the entire region.



118

119 **Figure 1:** Study area and domains of the numerical model. The coordinates of the different
 120 domains are as follows: D01: 98.23 E to 135.35 E, 23.45 N to 52.49 N; D02: 107.88 E to
 121 126.65 E, 30.91 N to 46.00 N; D03: 112.25 E to 121.23 E, 36.04 N to 43.19 N; D04: 115.17 E
 122 to 117.68 E, 39.21 N to 41.20 N. The grid spacing for each domain is 27 km, 9 km, 3 km, and 1
 123 km, respectively.

124

125 2.2. Data Descriptions

126 In the experiment, ERA5 global reanalysis data were used to provide initial and
 127 boundary conditions for the WRF model (Hersbach et al. 2020b). The data selected
 128 for this study has a temporal resolution of 1 hour and a spatial resolution of $0.25^\circ \times$
 129 0.25° . To investigate the impact of land use in the simulation, updated land use data
 130 were used to replace the default one within the WRF model. The data used in this
 131 study were acquired from the Moderate-resolution Imaging Spectroradiometer
 132 (MODIS) MCD12Q1 V6 product for the year of 2020, with a spatial resolution of 500
 133 m (Friedl 2019).

134 The gauge observations used to verify the model simulation on single points
 135 were from the China Meteorological Administration (version 2.0;
 136 <http://data.cma.cn/en>). There are totally 37 stations in the D04 area, shown in Figure

137 2(a). Due to the scarcity of meteorological stations, the observations were compared
138 with the model outputs on the grid that the meteorological stations located in. In order
139 to evaluate the quality of simulated precipitation depending on terrain, the stations
140 with altitude greater or smaller than 100 m are divided into mountainous stations and
141 plain stations, which have 10 and 27 stations respectively.

142 The analysis involves the movement and spatial variability of extreme
143 precipitation systems, which cannot be adequately captured by meteorological
144 observation stations. Alternatively, satellite-derived precipitation products are
145 commonly used and have reliabilities in estimating spatial precipitation distribution
146 (Bhattarai and Talchabhadel 2024). Among them, the Climate Prediction Center
147 Morphing technique (CMORPH) product can offer high temporal and spatial
148 resolution and has demonstrated advantages in capturing extreme precipitation
149 patterns (Liu et al. 2022), which has been validated over China in previous studies
150 (Ebert et al. 2007; Jiang et al. 2016; Sun et al. 2016). CMORPH data based on a
151 combination of microwave and infrared precipitation data provide high temporal and
152 spatial resolution global precipitation data (Joyce et al. 2004), and is highly
153 reasonable to be used to validate the simulation results. In this study, CMORPH data
154 with a temporal resolution of 30 min and spatial resolution of 8 km \times 8 km were used
155 for precipitation validation.

156

157 2.3. Model Description and Experimental Design

158 WRF model version 4.5.1 was selected as the numerical simulation tool for this
159 study (Skamarock 2019). The simulation period covered from 00:00 UTC July 28th,
160 2023 to 00:00 UTC August 2nd, 2023, while the first 24 hours were used for model
161 spin-up. A four-level nested domain was utilized with grid spacing (grid number) of
162 27 km (120 \times 122), 9 km (181 \times 187), 3 km (259 \times 268), and 1 km (217 \times 226).
163 Domain D01 covered most of central and eastern China, and domain D04 was focused
164 on the Beijing region (Figure 1). In addition, 49 vertical layers were employed in the
165 simulation and the upper boundary was set at 50 hPa to resolve the vertical structure

166 of the subtropical high and upper-level jet streams while minimizing spurious wave
 167 reflection near the upper boundary (Wang et al. 2018, Yu et al. 2024, Pei et al. 2025).
 168 The physical packages used are summarized in Table 1. To ensure that the large-scale
 169 circulation in the experiment closely matched the ERA5 input data for accurate results,
 170 spectral nudging was applied to the D01 domain in terms of the zonal and meridional
 171 wind, temperature, and specific humidity (Miguez-Macho et al. 2004; Spero et al.
 172 2014). The assimilation coefficient was set to $3 \times 10^{-4} \text{ s}^{-1}$ suggested in other previous
 173 researches (Holst et al. 2016; Liu et al. 2012; Ma et al. 2016; Pei et al. 2025), and the
 174 cut-off wave number was set to 3 in both the zonal and meridional directions as the
 175 length-scale is more accurate at 1000 km (Gómez and Miguez-Macho 2017; Kukulies
 176 et al. 2023). The hourly output for region D04 was used in the following analysis.

177

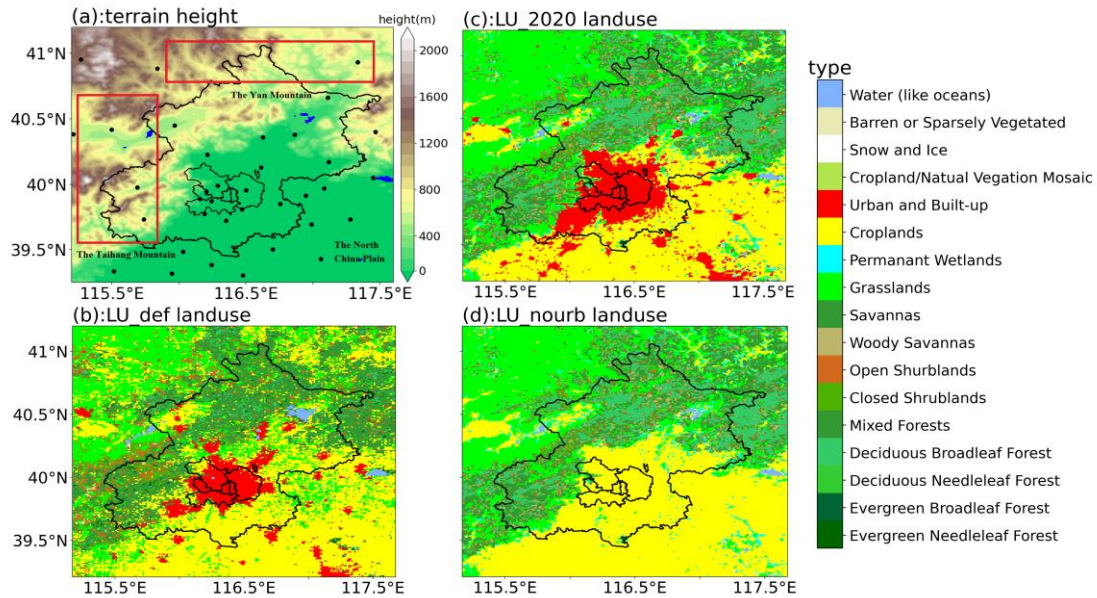
178

179

Table 1: Model configurations selected for WRF in this study

Options	Settings
Surface layer scheme	Mellor-Yamada-Janjic scheme (Janjić 1994)
PBL scheme	Yonsei University scheme (Hong et al. 2006)
Land Surface scheme	unified Noah land-surface model (Chen and Dudhia 2001)
Shortwave radiation	Dudhia scheme (Dudhia 1989)
Longwave radiation	RRTM scheme (Mlawer et al. 1997)
Microphysics scheme	WSM6 (Hong 2006)
Cumulus scheme	Kain-Fritsch scheme for D01 & D02 (Kain 2004)

180



181
 182 **Figure 2:** Terrain elevation and land use types in domain D04 in the experiment. (a) Terrain
 183 elevation in region D04. The dots represent the locations of meteorological stations used in this
 184 study. (b) Default land use types in region D04. (c) Land use types in region D04 after
 185 replacement. (d) Land use types in region D04 with urban areas replaced by cropland.

186

187 To improve the accuracy when simulating the impacts of urban areas on the
 188 precipitation event, the single-layer urban canopy model (Chen et al. 2011) was used
 189 to enhance the accurate simulation of the evolution of dynamic and thermodynamic
 190 processes in urban environments (He et al. 2023; Yu and Liu 2015). Different
 191 sensitivity test groups were set-up to explore the effects of land use and orography on
 192 the precipitation event, and the differences between these test groups were analyzed.
 193 The default land use types in WRF (represented as LU_def in Figure 2(b)) were
 194 replaced with land use data from the MODIS MCD12Q1 V6 product for the year
 195 2020 (represented as LU_2020 in Figure 2(c)).

196 To explore the impact of orography, based on the LU_2020 scheme, areas in
 197 domain D03 and D04 with elevations greater than 100 m were set to 100 m
 198 (represented as LU_nohgt) in order to explore the impacts of the Taihang and Yan
 199 Mountains on precipitation. In addition, urban areas in the land use data were replaced
 200 with cropland (represented as LU_nourb in Figure 2(d)) to examine the results in the
 201 absence of urban surface effects.

202

203 2.4. Verification Statistics

204 To investigate the impacts of land use changes on the simulation results, the
205 accumulated precipitation, precipitation intensity from LU_2020 simulations with
206 validated data were analyzed. The following evaluation metrics were used for
207 validation: mean absolute error (MAE), root mean square error (RMSE), and
208 correlation coefficient (R). The specific formulas for these metrics are as follows:

$$209 \quad MAE = \frac{1}{n} \sum_{i=1}^n |S_i - O_i| \quad (1)$$

$$210 \quad RMSE = \sqrt{\frac{\sum_{i=1}^n (S_i - O_i)^2}{n}} \quad (2)$$

$$211 \quad R = \frac{\sum_{i=1}^n (S_i - \bar{S})(O_i - \bar{O})}{\sqrt{\sum_{i=1}^n (S_i - \bar{S})^2 \sum_{i=1}^n (O_i - \bar{O})^2}} \quad (3)$$

212 where S_i and O_i are the simulated and observed values, respectively; \bar{S} and \bar{O} are the
213 average values of the simulated and validated data, respectively; and n is the number
214 of grid points.

215

216 3. Results

217 3.1. Evolution of the Precipitation Event

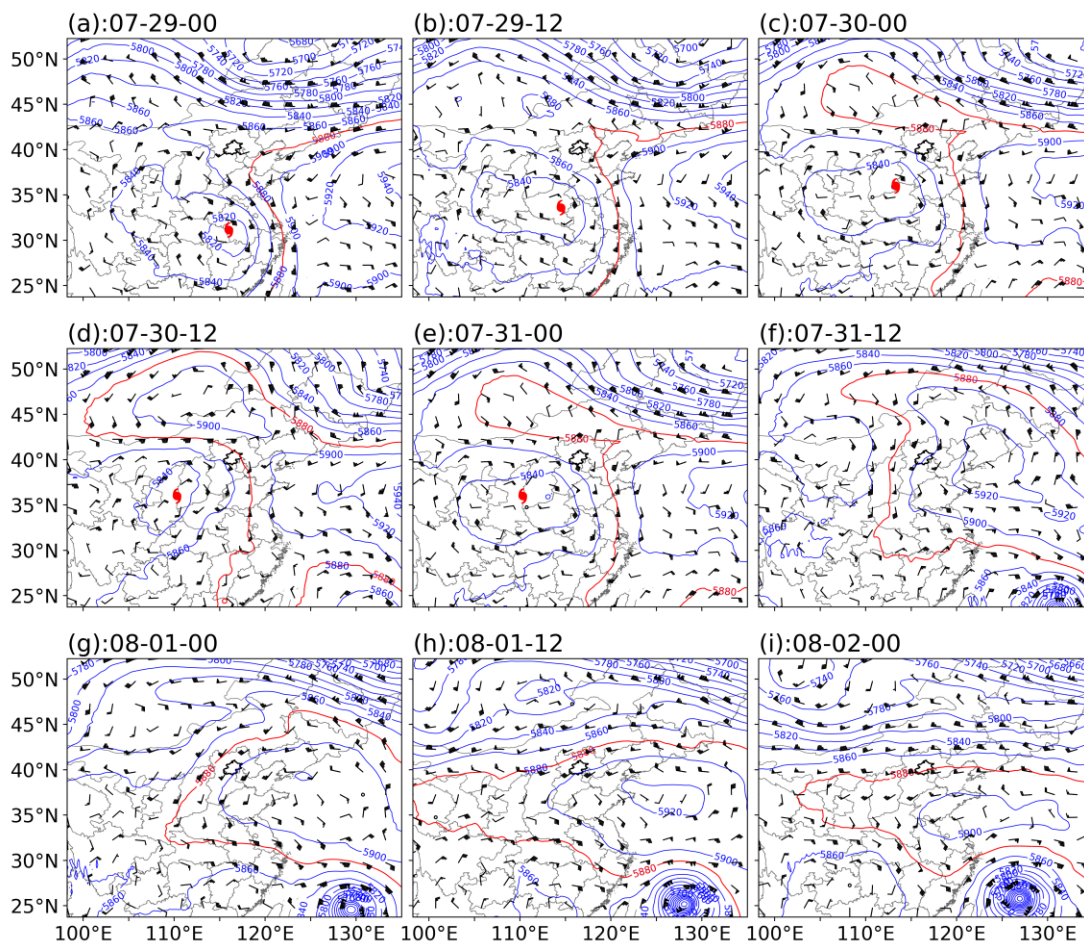
218 As shown in Figure 3, the remnant low of Typhoon Doksuri maintained
219 considerable intensity at the 500-hPa level on July 29, with its center located near
220 112 °–114 °E, 32 °–34 °N. At this time, the main body of the Western Pacific
221 Subtropical High (WPSH) was situated along the eastern coastal region of China and
222 the adjacent seas, with the westernmost position of the 5880-gpm geopotential height
223 contour around 118 °E, indicating its limited westward extension. The Beijing area
224 was primarily located within the weakly influenced northwestern periphery of the
225 WPSH, where low-level moisture transport was relatively weak and heavy
226 precipitation had not developed.

227 By July 30, the WPSH had extended westward, with the 5880-gpm contour
228 reaching approximately 105 °–110 °E and stretching northward to Mongolia. It thereby
229 established a relatively stable high-pressure ridge to the north of the Doksuri remnant
230 low and formed a typical blocking circulation pattern. Consequently, the center of the
231 remnant low oscillated slightly within 112 °–115 °E and 33 °–35 °N, illustrating a
232 pronounced quasi-stationary state that persisted until around 12:00 UTC July 31.
233 During this period, Beijing was located between the southern of the blocking high and
234 the northern of the remnant low. This configuration was favorable for sustained
235 southeast flow and continuous moisture toward Beijing area.

236 After 12:00 UTC July 31, the remnant low of Doksuri gradually weakened and
237 shifted slightly westward, while the blocking high also began to decay. Meanwhile,
238 Typhoon Khanun over the offshore waters of China (Figures 3(f)–(i)) established a
239 strong cyclonic circulation on its northwestern side, further enhancing moisture
240 transport into North China. It greatly increased precipitable water, thereby triggered
241 the heavy precipitation event between 12:00 UTC July 31 and 00:00 UTC August 1.
242 Then, the WPSH further intensified and continued to westward extension, with the
243 5880-gpm contour maintained at the west of 108 °E. The western ridge of the
244 strengthened WPSH subsequently blocked the moisture transport pathway from
245 Typhoon Khanun toward North China, leading to a pronounced reduction in the
246 moisture transportation. The precipitation process then gradually weakened and
247 terminated.

248 The differences among the experimental groups are mainly reflected in the local
249 circulation. A comparison of Figures S1 and S2 shows that the removal of terrain
250 elevation exerts a noticeable influence on the circulation associated with the remnant
251 low-pressure system. In the absence of the orographic blocking effect of the Taihang
252 Mountains, the remnant low of Typhoon Doksuri continued to move northward and
253 prolonged the duration of the low-pressure circulation. Consequently, the changed
254 dynamical and thermal conditions over the Beijing region were prone to alter the
255 spatiotemporal distribution of precipitation. In comparison, the differences between

256 Figures S1 and S3 indicate that urban underlying surface has a relatively weak effect
 257 on the large-scale circulation. It resulted in the reduction of the regional surface
 258 roughness and an increase in wind speed over Beijing area. In addition, the dissipation
 259 time of the remnant low circulation in the LU_nourb scheme is slightly prolonged due
 260 to the reduction of anthropogenic heat. Therefore, the large-scale circulation pattern in
 261 the LU_nohgt and LU_nourb schemes are generally similar to LU_2020. This
 262 suggests that the differences in simulated precipitation are primarily induced by the
 263 changes in local circulation.



264
 265 **Figure 3:** 500hpa circulation pattern for the precipitation event (source: ERA5). The blue solid
 266 lines represent geopotential height contours; the red solid contours represent position of
 267 subtropical high; the typhoon symbols in (a) - (e) represent residual circulation center of typhoon
 268 Doksuri.

269
 270 3.2. Analysis of Variations in Precipitation

271 3.2.1. Impacts of Updated Land Use Data

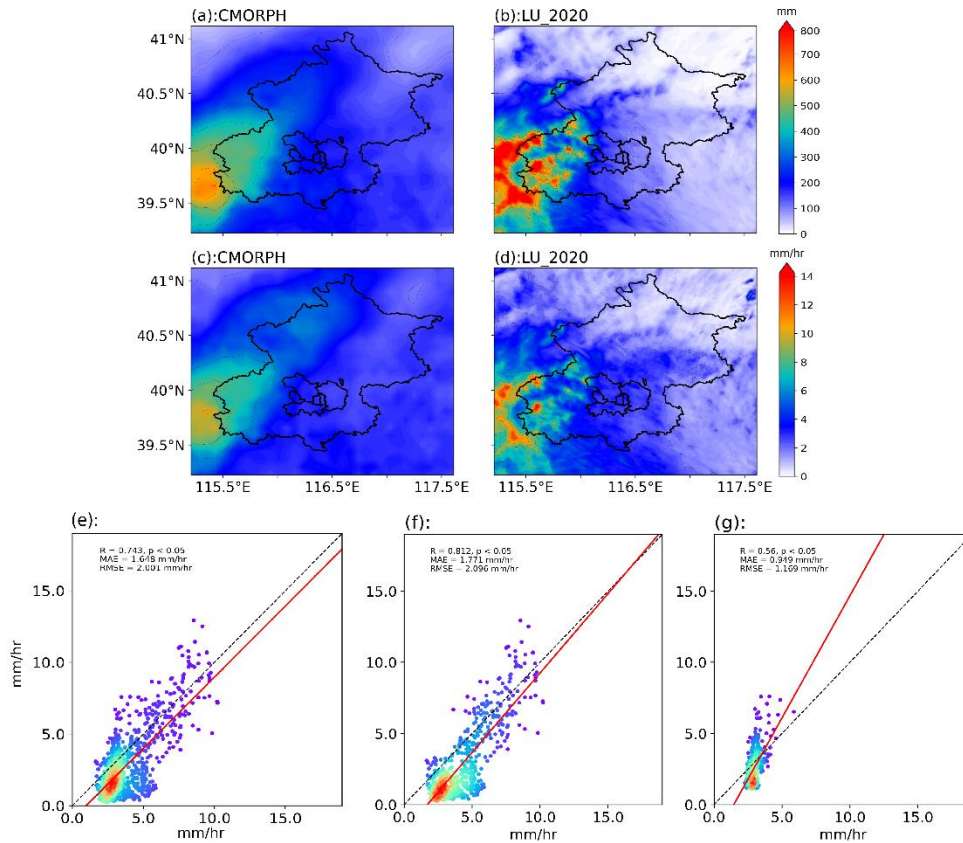
272 The simulated precipitation was compared with meteorological station

273 observations and satellite products to evaluate the accuracy of the model outputs. It
274 was found that, the maximum observed precipitation is 772.2 mm, which was
275 comparable with the simulation result of approximate 800.0 mm. The average
276 precipitation amount was 237.0 mm for all the station observations during this
277 precipitation event, and the average simulated value on the grid where the station
278 located in is 228.4 mm. Therefore, the magnitudes were comparable between model
279 simulation and observation on the stations.

280 The CMORPH data were used to further verify the spatial distribution of
281 precipitation on D04 region. As shown in Figure 4(a–b), the spatial distributions of
282 accumulated precipitation were similar, with higher precipitation in the southwestern
283 mountainous areas and lower precipitation in the northeastern region. This illustrated
284 that the pattern of LU_2020 scheme closely matched the accumulated precipitation
285 distribution obtained by CMORPH, which was slightly higher than 700 mm. The
286 simulated average precipitation intensity results also matched closely with the spatial
287 distribution of CMORPH (Figure 4(c-d)) although LU_2020 slightly underestimated
288 the precipitation intensity (Figure 4(e)). Thus, the WRF simulation results provided a
289 reasonable representation of the overall precipitation event, and the LU_2020
290 simulation results were used to analyze the differences due to orography and land use.
291 The correlation coefficient of the plain areas shows a smaller value ($R=0.56$)
292 compared with mountain areas ($R=0.81$). For the result of MAE and RMSE, the
293 statistics in the plain areas are smaller than those in the mountainous areas and the
294 entire study region (Table 2). This may be due to that there are more stations in the
295 plain areas, and the precipitation is smaller than mountain areas.

296 In addition, the model uncertainty was further accessed using an ensemble
297 simulation of LU_2020 scheme, where are originated from 10 ensemble members of
298 ERA5. They provide estimates of the short-range forecast uncertainty, and can be
299 considered to represent the evolution of the errors in the high-resolution component of
300 ERA5 (Hersbach et al. 2020a). The results show that there is slightly difference
301 between the ensemble mean simulation and our experimental results (Figure S4).

302 Statistically, the average precipitation intensity is 3.6 mm/hr for LU_2020 scheme and
 303 4.1 mm/hr for the ensemble mean. The RMSE and MAE of precipitation intensity is
 304 1.17 mm/hr and 0.86 mm/hr for the two simulation results and the correlation
 305 coefficient is 0.90. Therefore, the experimental scheme and simulation results in this
 306 study are convincing.



307
 308 **Figure 4:** Comparison of simulated and validated precipitation: (a)–(b) accumulated precipitation
 309 for CMORPH and LU_2020, respectively; (c)–(d) average precipitation intensity for CMORPH
 310 and LU_2020; and (e) scatter plots for the precipitation intensity for CMORPH in x axis and
 311 LU_2020 in y axis, while the red line represents the linear regression; (f) and (g) representing area
 312 where terrain height greater and smaller than 100 m.

313

314 Table 2: Statistics of the precipitation intensity between simulation and CMORPH data.

	R	RMSE (mm/hr)	MAE (mm/hr)
All	0.74	2.00	1.65
Mountain	0.81	2.10	1.77
Plain	0.56	1.17	0.95

315

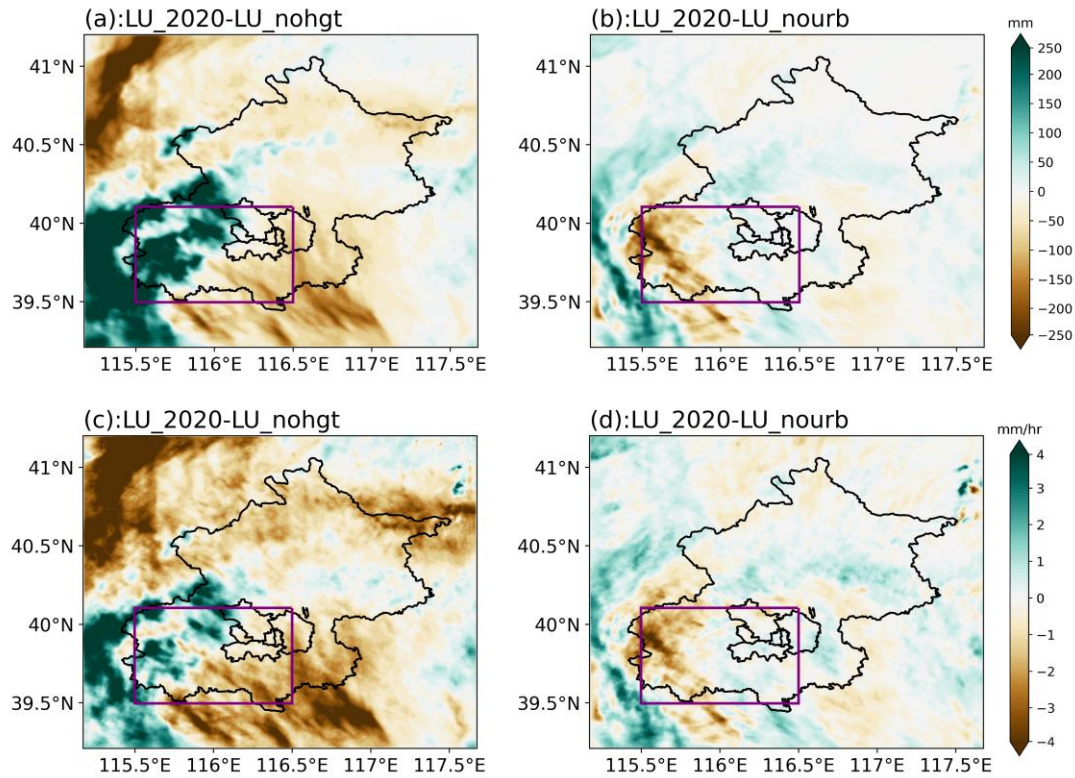
316

317 3.2.2. Impacts of Orography

318 Figure 5 (a) and 5(c) show the spatial distributions of the average precipitation

319 intensity and accumulated precipitation before and after removing the orography. It
320 illustrated that the removal of terrain elevation indeed significantly altered the spatial
321 pattern of accumulated precipitation throughout the simulation period. Compared to
322 the LU_2020 scheme, the LU_nohgt exhibited a marked decrease in cumulative
323 precipitation over the southwestern portion of D04 area. The accumulated
324 precipitation was 229.4 mm higher in LU_nohgt, accounting for over 41.34% of the
325 total precipitation. In contrast, in the central urban and northern regions of Beijing, the
326 total precipitation was 83.6 mm lower, representing 43.50% of the total precipitation.
327 This is primarily attributed to the removal of the Taihang mountainous region. As the
328 blocking effect caused by mountain on the remnant circulation was greatly diminished.
329 This allowed low-pressure system persist a long period within Beijing region and
330 facilitated its northward progression. The lack of orographic lifting ultimately leads to
331 different precipitation distributions over the Beijing region.

332 Figure 6(a) and 6(b) show the changes in precipitation for each time period at the
333 central latitudes between 39.5°N and 40.1°N. From 00:00 to 10:00 on July 30,
334 precipitation primarily occurred in the transition zone between the city and mountains,
335 where the terrain features caused heavy precipitation in the mountainous areas in the
336 morning during this period. From July 31 to 12:00 on August 1, precipitation mainly
337 occurred in the mountainous areas, and the impact of orography became more
338 significant. In the LU_nohgt scheme, precipitation in the mountainous areas stopped
339 around 12:00 on July 31, whereas in the LU_2020 scheme, precipitation continued
340 until around 00:00 on August 1, i.e., 12 hours longer. Thus, the topography had a
341 significant impact on the second phase of precipitation. In terms of the precipitation
342 intensity and distribution, the presence of the orography altered the timing of heavy
343 precipitation in the mountainous areas and intensified the precipitation in the central
344 urban area around 12:00 on July 31.



345
 346 **Figure 5:** Effects of terrain and urban underlying surface changes on accumulated precipitation
 347 and average precipitation intensity from 00:00 July 29th to 00:00 UTC August 2nd: (a) and (c)
 348 differences in accumulated precipitation and average precipitation intensity between the
 349 simulation using 2020 land use data and the scheme where terrain higher than 100 m was removed;
 350 and (b) and (d) differences in accumulated precipitation and average precipitation intensity
 351 between the simulation using 2020 land use data and the scheme where urban land use was
 352 removed. The purple area (RegP) indicates the region in Beijing where the difference in
 353 precipitation was significant.

354

355 3.2.3. Impacts of Land Use

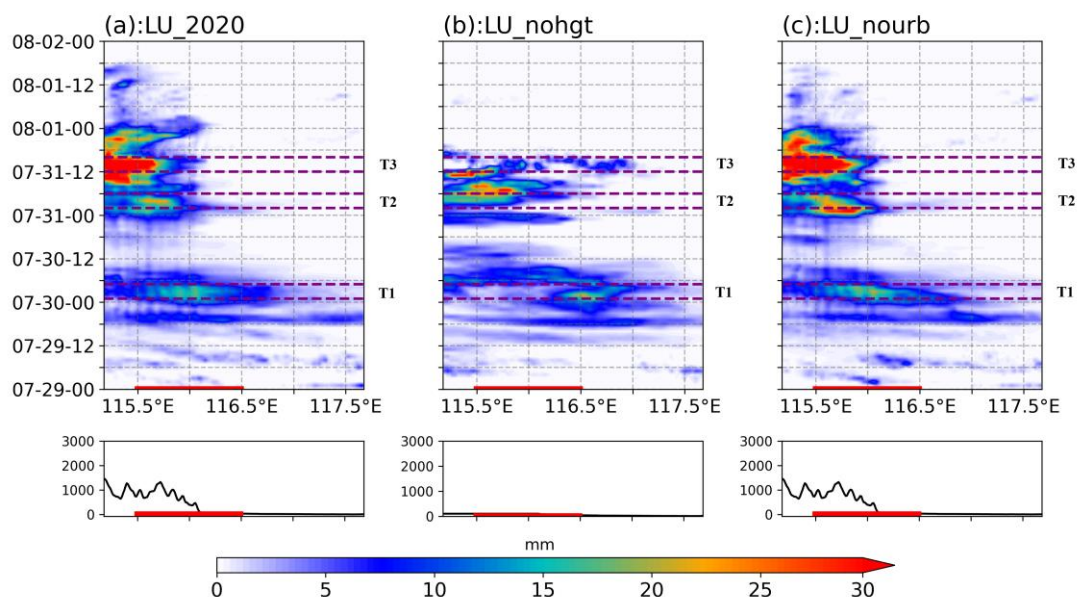
356 Figure 5(b) and 5(d) show the impact of the urban land surface compared with
 357 removal of the urban land surface. The spatial distributions of the average
 358 precipitation intensity and accumulated precipitation were quite similar between
 359 LU_2020 and LU_nourb, with no significant difference in the overall precipitation
 360 pattern. The presence of urban areas did not significantly affect the central urban
 361 region of Beijing. However, in the southwestern mountainous region of Beijing, the
 362 average accumulated precipitation was 88.1 mm lower (the total precipitation was
 363 15.87% lower).

364 Figure 6(a) and 6(c) show the variations in precipitation with longitude and time

365 for the central urban region corresponding to the central latitude. From 00:00 to 10:00
 366 on July 30, the range and intensity of precipitation differed little between the city and
 367 the mountain transition zone, indicating that changes in land use had minor effects
 368 during this period. From July 31 to 12:00 on August 1, the overall total precipitation
 369 was lower in the LU_2020 scheme, although more precipitation occasionally occurred
 370 in the western part of the city in the LU_2020 scheme compared with the LU_nourb
 371 scheme. There was no significant difference in the duration of precipitation between
 372 the two experimental groups.

373 Therefore, during the precipitation event, both orography and land use altered the
 374 precipitation pattern, where the most significant changes in precipitation occurred in
 375 the southwestern part of Beijing. To understand the main causes of the differences in
 376 precipitation, the region denoted by the purple box in Figure 5 was selected for more
 377 detailed analysis of the underlying mechanism as it was affected most by the land
 378 surface (referred to as RegP hereinafter). In addition, due to the prolonged nature of
 379 the event, three time periods with notable differences in the precipitation distribution
 380 according to Figure 5 were selected for further mechanistic analysis to explore the
 381 effects of orography and land use on the event. The three periods of interest were:
 382 01:00–04:00 UTC on July 30th (referred to as T1), 03:00–06:00 UTC on July 31st
 383 (referred to as T2), and 12:00–15:00 UTC on July 31st (referred to as T3).

384



385

386 **Figure 6:** Hovmöller diagrams from 00:00 July 29th to 00:00 UTC August 2nd for the three
387 experimental groups: (a) LU_2020 scheme, (b) LU_nohgt scheme, and (c) LU_nourb scheme,
388 within the range of 39.8 N–40.1 N. Terrain heights at corresponding latitudes are shown.

389

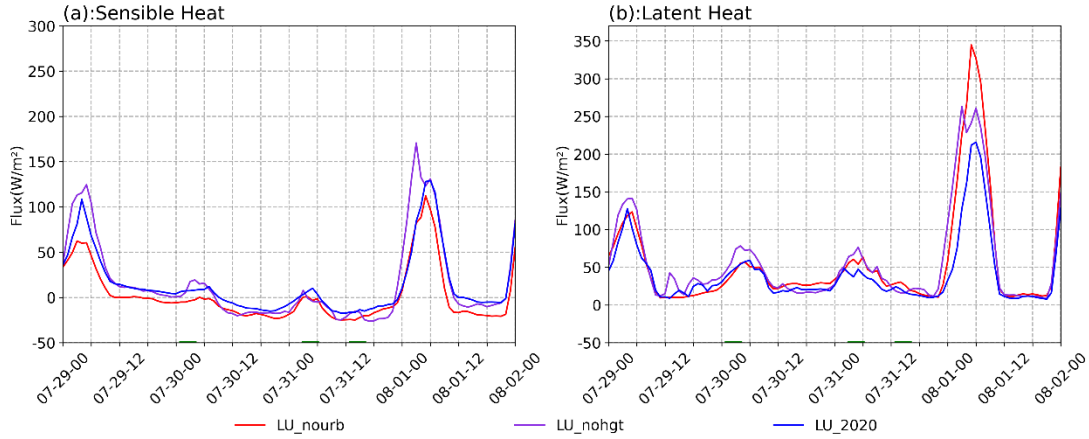
390 3.3. Physical Mechanism

391 3.3.1. Energy and Water Vapor Budget Comparison

392 The energy and water vapor fluxes were compared among different experimental
393 groups. As shown in Figure 7, all experimental groups exhibited distinct diurnal
394 variations, with significant increases in both the sensible heat flux and latent heat flux
395 after 00:00 UTC August 1st. This phenomenon was mainly due to the end of the
396 extreme precipitation event, where the increased surface energy input strengthened
397 both the sensible and latent heat fluxes. In RegP, both the sensible and latent heat
398 fluxes were slightly higher than the regional averages. The orographic effects on the
399 latent heat flux were more pronounced, especially during periods T1 and T2 (Table 3),
400 as the removal of orographic features lead to an increase in both surface pressure and
401 temperature for the high elevated regions. It enhances near-surface humidity and
402 alters the latent heat flux across the region. The relatively lower latent heat flux
403 observed in LU_nohgt during period T3 could be attributed to the extended duration
404 of the precipitation event, which was caused by the removal of orography.

405 Compared with period T1, urbanization reduced latent heat flux by an average of
406 16.70 W/m^2 and 7.06 W/m^2 in RegP during periods T2 and T3, respectively. This was
407 mainly because the lower permeability of urban surfaces compared with croplands
408 reducing the regional humidity, and thus decreasing the latent heat flux across the area.
409 The impact of urbanization on the moisture content in RegP was less pronounced
410 during period T1, suggesting that removing urban areas had minimal effect on the
411 water vapor content. Changes in the sensible heat flux (Figure 7(a)) due to
412 urbanization were also concentrated in RegP, since the orography in the urban area
413 varied little among the three experimental groups. When the land use shifted from
414 urban surfaces to croplands, the reduced urban heat emissions significantly decreased
415 the sensible heat flux in the central urban area, so it was lower than that in the other

416 groups. It was notable that changes in the latent heat flux (Figure 7(b)) in RegP were
 417 more complex than those in the sensible heat flux, which could be attributed to
 418 different changes in the water vapor content.



419
 420 **Figure 7:** Temporal variations in energy balance during the event for the LU_2020, LU_nohgt,
 421 and LU_nourb schemes. In (a) and (b), solid lines represent the sensible and latent heat fluxes
 422 within the precipitation anomaly area RegP for each scheme.

423
 424
 425

Table 3: Average flux values in RegP region during precipitation process (unit: W/m²)

flux	Scheme	T1	T2	T3	All-time
Sensible Heat	LU_2020	7.28	5.98	-15.36	14.04
	LU_nohgt	10.85	-0.62	-18.47	16.25
	LU_nourb	-4.19	-0.92	-22.91	1.83
Latent Heat	LU_2020	46.38	41.82	19.04	41.85
	LU_nohgt	63.38	67.18	17.68	58.00
	LU_nourb	42.74	58.52	26.10	56.29

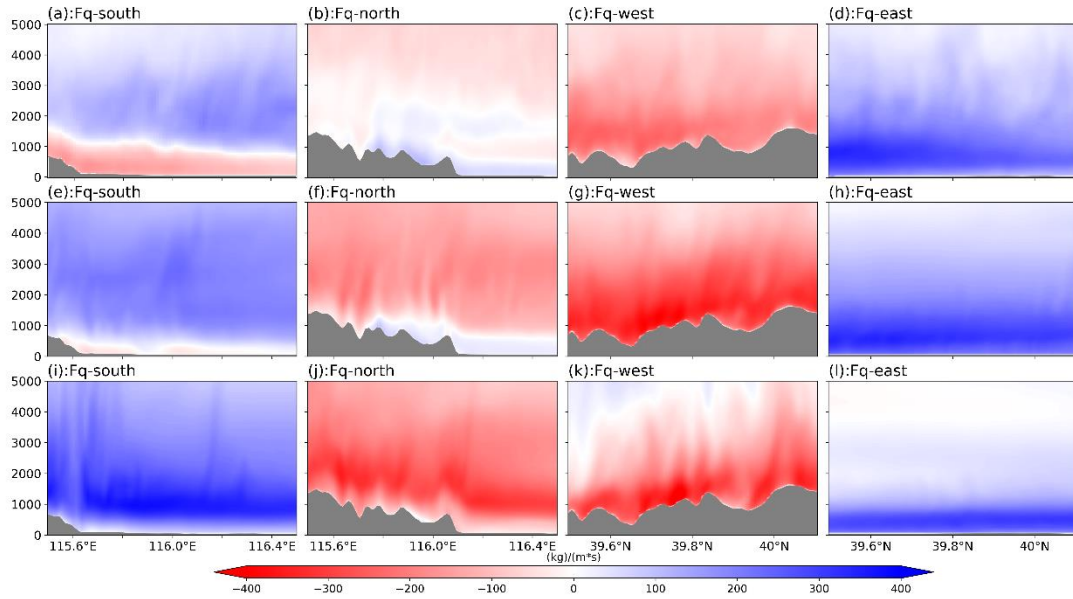
426

427 Figure 8 shows the magnitudes of the water vapor flux at the four boundaries of
 428 RegP for LU_2020. An increase in net moisture convergence during each period leads
 429 to higher precipitable water over the region, which in turn provides more favorable
 430 conditions for precipitation. Specifically, the moisture inflow across the southern
 431 boundary (Figure 8(a), (e), (i)) and the eastern boundary (Figure 8(d), (h), (l))
 432 represents meridional and zonal sources of water vapor entering the region. The
 433 outflow across the northern boundary (Figure 8(b), (f), (j)) and the western boundary
 434 (Figure 8(c), (g), (k)) reflects the moisture exported from the region. The difference

435 between the inflow and outflow moisture flux indicates net moisture income in each
436 time period (shown in Table 4).

437 During period T1, about 49.58 kg/(m s) water vapor was transported southward
438 at lower latitudinal levels along the southern boundary, while it was transported
439 totally 58.63 kg/(m s) northward at high latitudes. As the Taihang Mountains extend
440 in a southwest-northeast direction in the study area, the eastern zonal airflow was
441 totally 130.50 kg/(m s), blocked by the Mountainous area and shifted southward
442 which explained why water vapor was transported southward in northern boundary.
443 Overall, the moisture input into the RegP was dominated by zonal water vapor
444 transport. Although the meridional transport contributed a relatively large amount of
445 moisture inflow, its substantial outflow resulted in a comparatively small net
446 contribution to the regional moisture budget.

447 The water vapor flux distributions were similar during periods T2 and T3, while
448 the magnitude of water vapor decreased from 23.58 kg/(m s) to 6.25 kg/(m s).
449 Although the zonal water vapor transport increased to some extent, the total moisture
450 inflow during the two periods remained comparable. Meridionally, the eastward water
451 vapor flux decreased from -13.97 kg/(m s) to -23.71 kg/(m s). In addition, the water
452 vapor transport during T3 became more concentrated in the lower layers which
453 indicated the contribution of low-level water vapor transport to the precipitation
454 process. Compared with that in T1, the northward water vapor flux at the southern
455 boundary was significantly increased in T2 and T3. The northwestward transport
456 increased and led to strong uplift motion in the mountainous area. Consequently, the
457 mountainous areas may have been more prone to intense convective weather events
458 due to the sufficient water vapor and air uplift during T2 and T3.



459

460

461

462

463

464

465

466

467

468

469

470

471

472

473

474

475

476

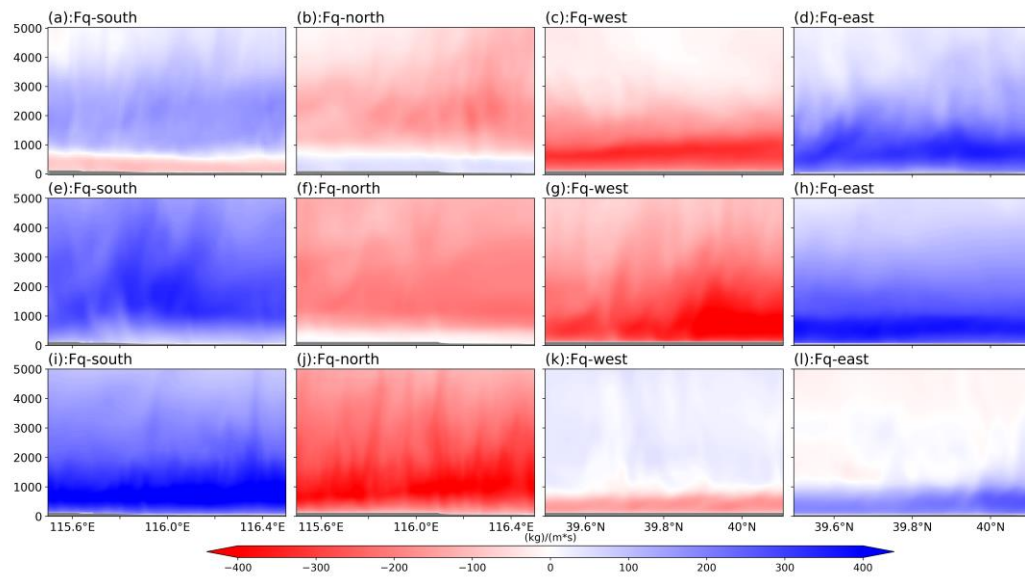
477

478

479

Figure 8: Distribution of water vapor flux magnitude in the LU_2020 scheme across latitude-height/longitude-height coordinates of RegP. Figures show the water vapor flux magnitude for time periods T1 (a - d), T2 (e - h), and T3 (i - l), with fluxes from the south (a, e, i), north (b, f, j), west (c, g, k), and east (d, h, l). Positive and negative water vapor flux values correspond to input and output water vapor flux relative to RegP.

Orographic height significantly impacted water vapor flux transport, as shown by the differences in the water vapor distribution between LU_2020 (Figure 8) and LU_nohgt (Figure 9) and the corresponding water vapor flux transport in Table 4. From a zonal perspective, orography considerably influenced the water vapor distribution within RegP. Due to orographic effects, water vapor was lifted and its northward transport was prevented, statistically reduced about 63.57 kg/(m s) in the LU_2020 (Figure 9 (a), (e), (i)), which also increased the total amount of zonal water vapor flux in LU_2020. From meridional perspective, the meridional water vapor flux output from western boundary substantially decreased by 49.41 kg/(m s) and 79.38 kg/(m s) during the whole period, resulting in a noticeable rise in the water vapor content in the entire region. Furthermore, the easterly winds were blocked and diverted by the orographic effect of the mountains to the west of Beijing, which also leads to a modest increase in the magnitude of the southward water vapor flux at the southern boundary in the lower atmospheric layers.



480

481 **Figure 9:** Water vapor fluxes as shown in Figure 8, where a - l depict the magnitude of the water
 482 vapor flux from four directions in the LU_nohgt scheme.

483

484 The impacts of the urbanization on water vapor transport are shown in Figure 10.

485 There was no significant difference between LU_2020 and LU_nourb in water vapor

486 flux during periods T1 and T2 as the difference between net convergence is smaller

487 than 10 kg/(m s). However, the differences mainly appeared at the western boundaries

488 of RegP during period T3. At the western boundary, the westward water vapor flux

489 was 30.98 kg/(m s) higher compared with that in LU_nourb (Figure 10(k)). These

490 differences of moisture flux between different schemes were mainly due to wind

491 speed in lower troposphere. As urban land use can influence local atmospheric

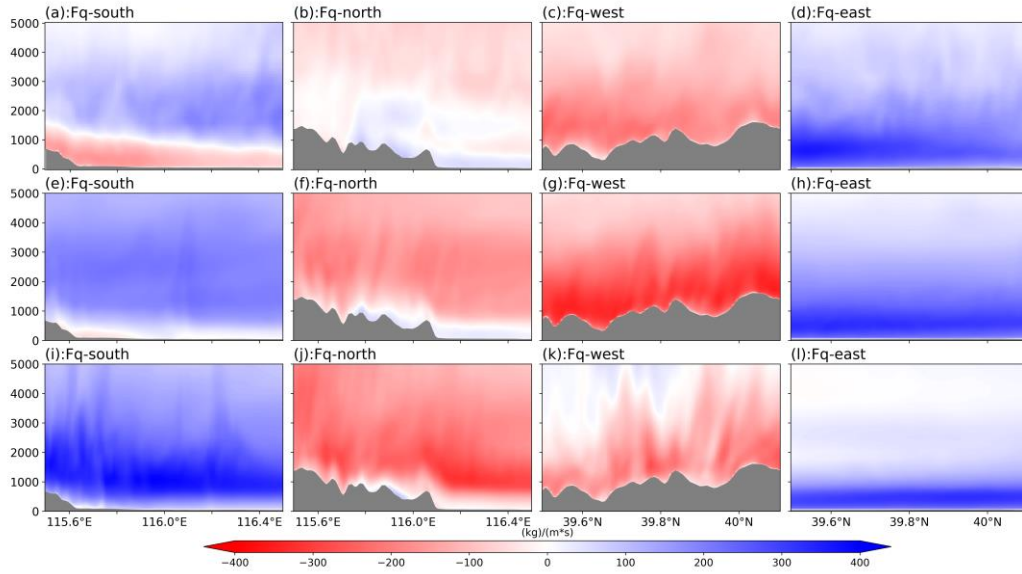
492 circulation, such strong ascent induces horizontal convergence and a subsequent

493 conversion of horizontal momentum into vertical motion. Such momentum

494 redistribution can reduce the horizontal wind speed, particularly within the

495 convectively active region, leading to a reduction in moisture flux across the western

496 and northern boundaries.



497

498 **Figure 10:** Water vapor fluxes as shown in Figure 8, where a - l depict the magnitude of the water
 499 vapor flux from four directions in the LU_nourb scheme.

500

501

Table 4: The water vapor flux (kg/(m s)) during each period for different schemes.

	kg/(m s)	North	South	Zonal	West	East	Meridional	All
T1	LU_2020	58.63	-19.52	39.11	130.50	-100.61	29.89	69.00
	LU_nohgt	78.89	-83.09	-4.20	141.79	-110.93	30.86	26.66
	LU_nourb	55.42	-22.42	33.00	133.97	-94.19	39.78	72.78
T2	LU_2020	146.94	-109.39	37.55	146.05	-160.02	-13.97	23.58
	LU_nohgt	222.99	-146.99	76.00	176.09	-199.31	-23.22	52.78
	LU_nourb	152.31	-113.83	38.48	139.02	-150.29	-11.27	27.21
T3	LU_2020	199.32	-169.36	29.96	71.65	-95.36	-23.71	6.25
	LU_nohgt	228.22	-237.85	-9.63	32.12	-0.69	31.43	21.80
	LU_nourb	206.16	-160.40	45.76	74.65	-64.38	10.27	56.03

502

503 3.3.2. Differences in Near-surface Physical Variables

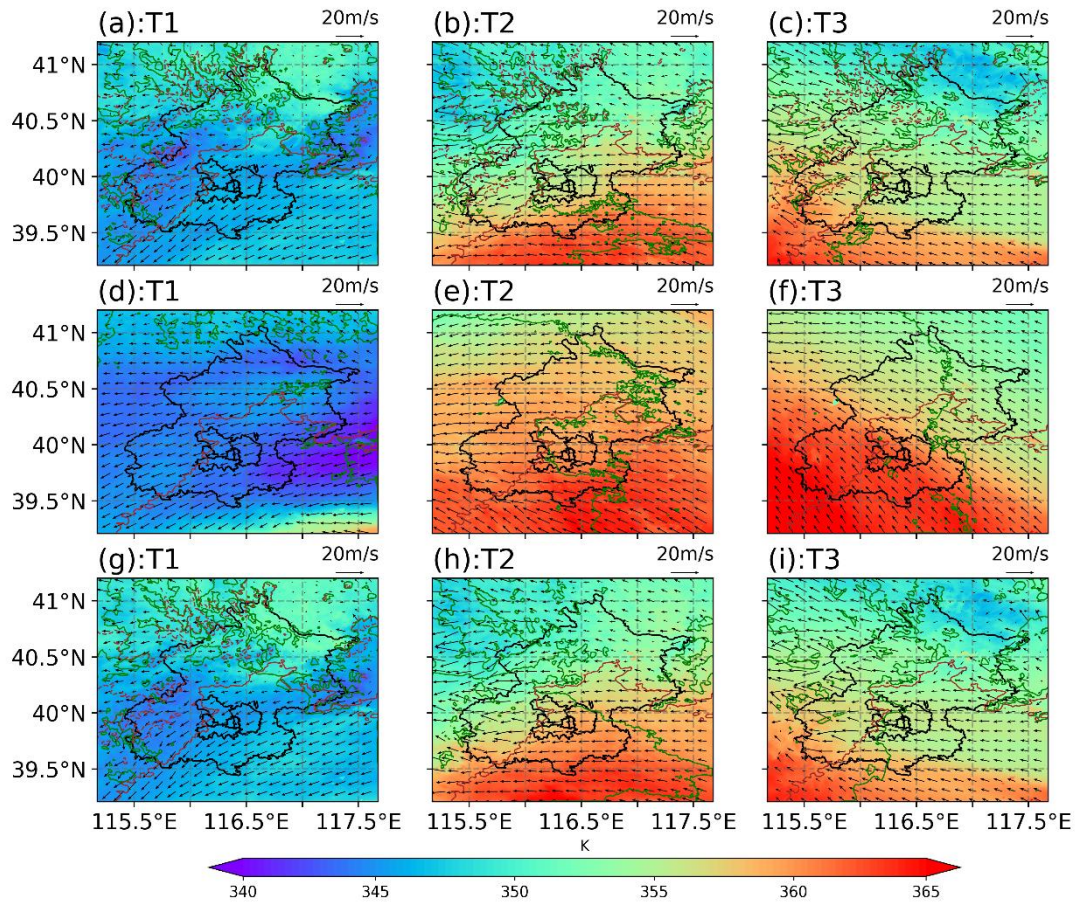
504 Near-surface physical quantities did not directly determine the magnitude of
 505 precipitation, but the changes in the underlying surface were directly reflected in
 506 variations in near-surface physical quantities, which then influenced the upper
 507 atmosphere and subsequently affected the intensity of precipitation. Figure 11(a–c)
 508 illustrates the horizontal distributions of the equivalent potential temperature, wind
 509 speed, and the humidity during the three precipitation time periods.

510 During period T1 (Figure 11(a)), precipitation was mainly concentrated in the
 511 southwestern mountainous and central region. The equivalent potential temperature
 512 over Beijing remained between 346 and 347 K, but it was slightly lower than the

513 regional average in RegP. These results are consistent with the flux changes shown in
514 Figure 7. The lowest equivalent potential temperature in Beijing was observed in the
515 northwestern mountainous region (343 K). In addition, the 2-m relative humidity in
516 Beijing during period T1 remained at an average value above 90%, and the 10-m
517 wind direction was influenced by the circulation and orographic blocking, resulting in
518 a northeastern wind. The wind direction was more erratic in the mountainous areas,
519 where the relative humidity was slightly lower than that in the plains, and the
520 precipitation was also relatively lower compared with the southern regions.

521 During period T2 (Figure 11 (b)), the precipitation entered the initial stage of the
522 second precipitation phase, during which the precipitation mainly occurred in the
523 southwestern mountainous areas. The warm and moist southerly air currents
524 transported water vapor and also provided the energy required for precipitation. The
525 equivalent potential temperature was higher in southern Beijing, and it decreased from
526 south to north, a trend linked to the energy loss as the air moved northward. This
527 variation was associated with the energy dissipation process as the airflow moved
528 northward. The overall equivalent potential temperature gradually increased over time,
529 from 351.6 K at 03:00 UTC on July 31 to 354.3 K at 06:00 UTC on July 31.

530 In period T3 (Figure 11(c)), the precipitation remained intense and the areas with
531 the most intense precipitation were still located in the western mountainous areas of
532 Beijing. The overall distribution of the equivalent potential temperature during this
533 period was similar to that in period T2, and the highest values were still located in the
534 southwestern mountainous areas of Beijing. The average equivalent potential
535 temperature in Beijing remained within a range of 355K to 356 K. The overall relative
536 humidity in the region was higher compared with that in period T2 (rising to 90.0%).
537 The wind direction in the central urban area shifted slightly to the north due to the
538 influence of the northerly air currents, but there was no significant change in the wind
539 speed compared with that in period T2.



540
 541 **Figure 11:** Simulated 2-m equivalent potential temperature, 2-m relative humidity, 10-m wind
 542 speed, and orographic height for LU_2020 scheme (a–c), LU_nohgt scheme (d–f), and LU_nourb
 543 scheme (g–i). Three consecutive time periods were selected: T1 (a, d, g), T2 (b, e, h), and T3 (c, f,
 544 i). In the figures, the 2-m temperature is represented by color-filled maps, areas with 2-m relative
 545 humidity greater than 90% are outlined by green dashed lines, the 10-m wind speed is represented
 546 by arrows, brown solid lines indicate orographic contours at 100 m, and brown dashed lines
 547 represent orographic contours at 1000 m.

548

549 The effects of orography on the wind speed, temperature, and humidity were
 550 evident (Figure 11(d–f)). During period T1, the equivalent potential temperature in the
 551 LU_2020 scheme over Beijing was significantly higher compared with that in the
 552 LU_nohgt scheme, with the largest increase observed in the eastern and northeastern
 553 regions of Beijing. Due to the blocking effect of the mountains, the relative humidity
 554 across the entire D04 area also increased during period T1. During periods T2 and T3,
 555 the presence of the mountain range led to a notable decrease in the equivalent
 556 potential temperature across the region compared with the LU_nohgt scheme, mainly
 557 due to the transport of water vapor along the Taihang Mountains to the Beijing area

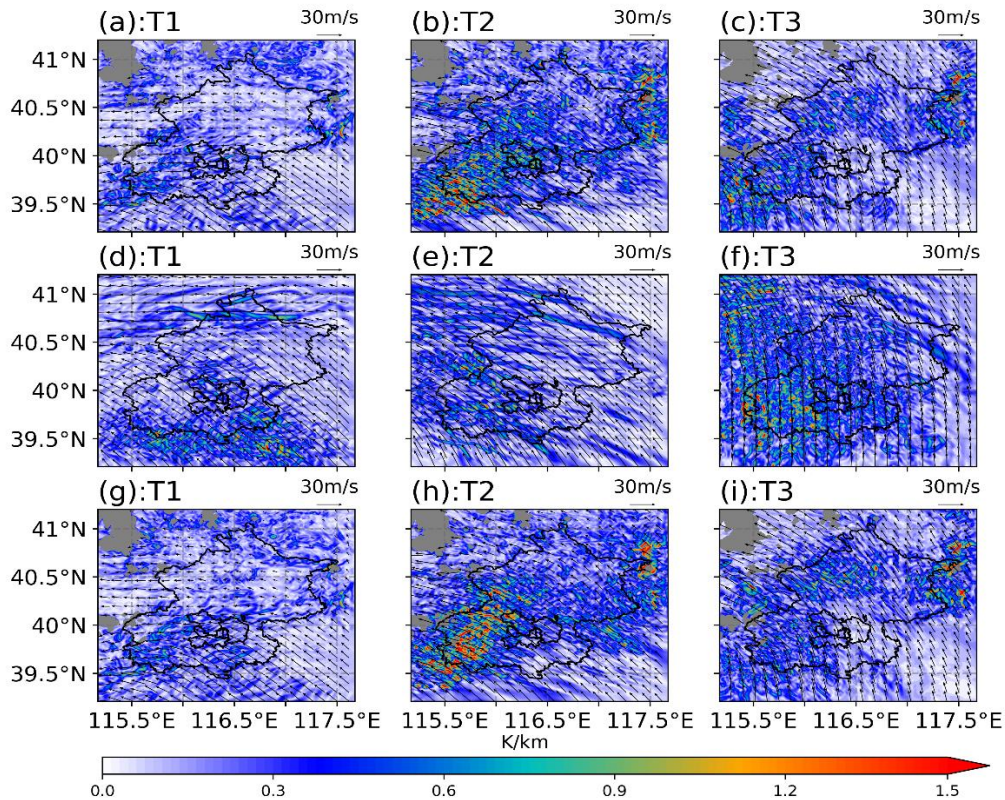
558 during the second stage, during which substantial amounts of water vapor and energy
559 accumulated as the air mass passed through the mountains. The dissipation of energy
560 and water vapor during this process led to significant reductions in the relative
561 humidity and equivalent potential temperature in the plains and northern Beijing
562 regions during these periods. Moreover, the presence of the western mountainous
563 terrain led to the redistribution of the water vapor, resulting in significant variability
564 in the humidity distribution in the mountainous areas. Minimal variation was found in
565 the overall wind direction in the plains, and there were no significant differences
566 between the two experimental groups across all three periods. However, in the
567 mountainous areas, the orography induced air convergence at the boundary between
568 the plains and mountains. Due to the complexity of the terrain, the wind speed and
569 direction were more heterogeneous in the western mountainous areas.

570 The effects of urbanization were analyzed by comparing LU_2020 (Figure 11(a–
571 c)) and LU_2020_nourb (Figure 11(g–i)). The changes in precipitation were primarily
572 concentrated in periods T2 and T3. During period T2, replacing urban underlying
573 surfaces with croplands significantly altered the 2-m relative humidity in the central
574 urban area, with an increase of more than 5%. This increase in the relative humidity
575 led to greater accumulation of latent heat in the air, and the 2-m equivalent potential
576 temperature in the central urban area increased by approximately 1 K as a result. The
577 wind speed increased slightly in the urban area, with greater air convergence in the
578 mountainous regions. During period T3, the increase in the relative humidity in the
579 urban area was smaller compared with that in period T2 (increasing by around 3%).
580 Wind convergence was still evident in the western mountainous regions. In particular,
581 although the relative humidity in the central urban area increased significantly, there
582 was no noticeable increase in the relative humidity in the downstream mountainous
583 areas located to the east of the urban region.

584 Since presenting only the surface equivalent potential temperature could be
585 insufficient to fully explain the influence mechanisms of the underlying surface, the
586 gradient of equivalent potential temperature at representative times is further analyzed

587 to characterize the atmospheric stability (Figure 12). The orographic lifting exerts a
588 significant modulation on the spatial distribution of the horizontal equivalent potential
589 temperature gradient. During the T1 period, the LU_nohgt scheme exhibits an
590 eastward displacement of the maximum gradient compared with the LU_2020,
591 accompanied by a noticeable shift in the 850-hPa wind shear location. This indicates
592 that, orographic lifting alters the low-level flow and thermodynamic structure, thereby
593 modulates the distribution of moist baroclinicity and the position of the potential
594 frontal zone. Therefore, it can provide a more favorable thermodynamic environment
595 for convective development over the mountainous areas. During the T2 period,
596 orographic lifting further enhances low-level moist baroclinicity and makes the high-
597 gradient zone more continuous. Combined with the low-level wind shear, these
598 conditions are conducive to frontogenetic processes and convective systems.

599 In contrast, although relatively large gradients still exist in the LU_nohgt during
600 the T3 period, the low-level convergence and vertical ascent are substantially
601 weakened. It prevents the effective release of thermodynamic instability, and therefore
602 the precipitation process consequently comes to an end. Meanwhile, the changes in
603 urban land use also influence the precipitation intensity, especially during the T2
604 period. The LU_2020 scheme exhibits larger horizontal gradients over the
605 southwestern mountainous region than LU_nourb. This indicates that urbanization can
606 enhance low-level moist baroclinicity in this area, which is favorable for
607 strengthening frontal structures and increasing the likelihood of intense convection
608 precipitation.



609

610 **Figure 12:** Gradient of equivalent potential temperature field for LU_2020 scheme (a–c),
 611 LU_nohgt scheme (d–f), and LU_nourb scheme (g–i) from 850 hPa. Three consecutive time
 612 periods were selected: T1 (a, d, g), T2 (b, e, h), and T3 (c, f, i)

613

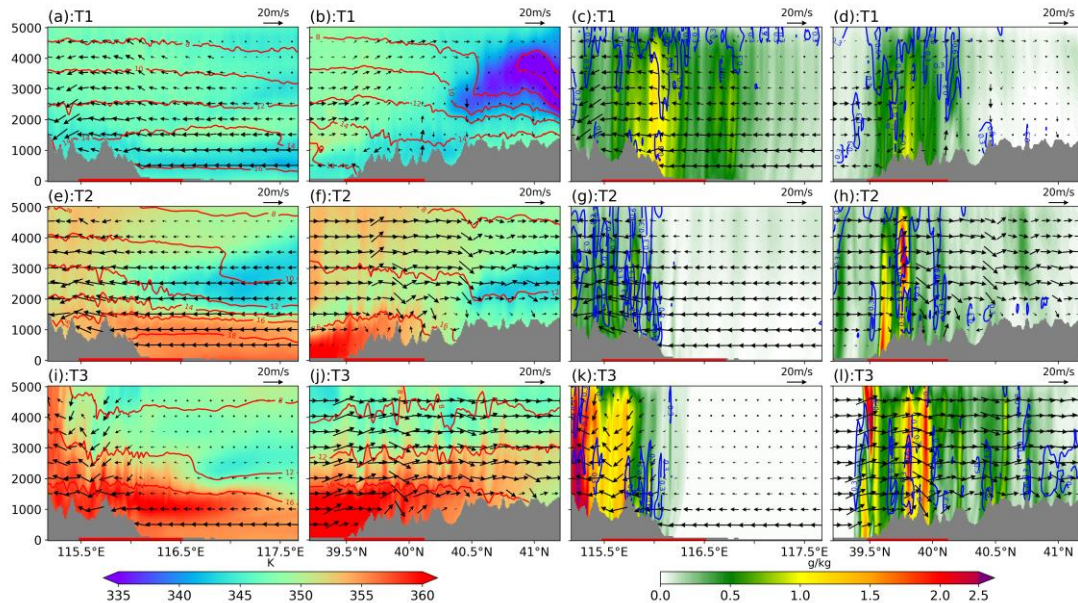
614 3.3.3. Differences in the Vertical Profile

615 Figure 13 presents the meridional and zonal vertical profiles for the three distinct
 616 time periods. In the LU_2020 scheme, convection was primarily confined to the
 617 mountainous regions and the plains to the east of the mountains during period T1. The
 618 orography blocking effect resulted in significant upward motion in both the
 619 mountainous areas and adjacent plains. Around 02:00 on July 30, the eastward water
 620 vapor flux was sufficiently high, leading to condensation of substantial amounts of
 621 water vapor into cloud droplets and raindrops over the mountainous regions. The
 622 latent heat released in this process induced fluctuations in the equivalent potential
 623 temperature contours in the upper levels. In the zonal direction, cloud droplets and
 624 raindrops were predominantly located over the southern mountains. In the northern
 625 mountainous areas, due to the relatively low water vapor flux and lower equivalent
 626 potential temperature, there was almost no vertical motion in the air, resulting in

627 negligible cloud droplet formation in this region.

628 During period T2, the atmosphere over the mountainous regions was
629 characterized by vigorous convection in the meridional direction. In the southwestern
630 mountains, higher equivalent potential temperatures correlated with greater cloud
631 droplet concentrations. Both the southerly winds and vertical wind speeds increased
632 significantly compared with those in period T1, and the cloud water and rainwater
633 mixing ratios were elevated near 39.8°N. The cloud water mixing ratios were
634 relatively high in other regions but this corresponded to the early stages of
635 precipitation when cloud water had yet to fully transition into rainwater, resulting in
636 low rainwater concentrations in most areas.

637 In the meridional direction, only the low-level wind speed over the plains was
638 noticeably higher in period T3 compared with that in period T2. The low-level winds
639 exhibited convergence, whereas the upper-level winds exhibited divergence in the
640 southwestern mountainous region, and thus the equivalent potential temperature
641 remained relatively high near the surface. In the zonal direction, notable convection
642 occurred over the mountainous areas, accompanied by significant fluctuations in the
643 near-surface equivalent potential temperature. In addition, the southward water vapor
644 flux was relatively large during this period, and the energy, water vapor, and motion
645 within the southwestern mountainous regions were conducive to the development of
646 convection. As illustrated in Figure 13(i–k), both the cloud water and rainwater
647 concentrations in the southwestern mountainous area increased compared with other
648 regions. Consequently, the region experienced relatively higher precipitation during
649 period T3.

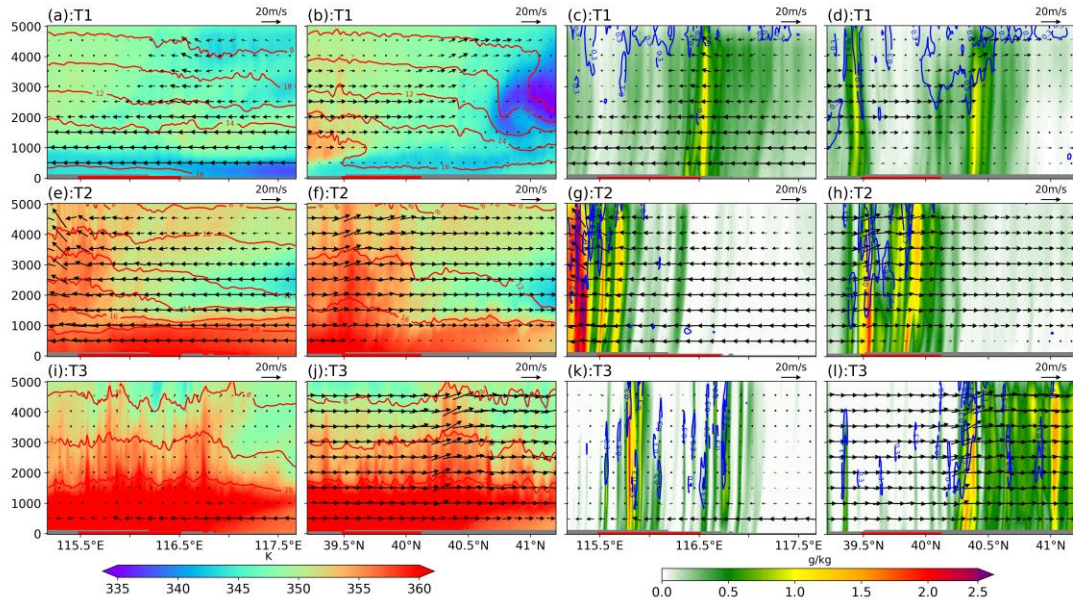


650
 651 **Figure 13:** Meridional-vertical profiles (a, c, e, g, i, k) at 39.9°N and zonal-vertical profiles (b, d, f,
 652 h, j, l) at 115.7°E for LU_2020. In (a, b, e, f, i, j), the shaded areas represent the magnitude of the
 653 equivalent potential temperature and red contours indicate the water vapor mixing ratio. In panels
 654 (c, d, g, h, k, l), the shaded areas represent the rainwater mixing ratio and blue contours indicate
 655 the cloud water mixing ratio. The arrows represent the horizontal wind vectors (with the vertical
 656 wind speed amplified by a factor of five). Gray shading denotes the terrain height. The red line at
 657 the bottom of the map indicates RegP, as shown in Figure 6.

658

659 Comparisons between the LU_2020 (Figure 13) and LU_nohgt (Figure 14)
 660 experimental groups highlighted the convection observed during the three periods
 661 driven by orographic uplift. In period T1, the uplift motion in the southern part of the
 662 area facilitated the condensation of cloud droplets and raindrops, thus increasing the
 663 precipitation intensity. In period T2, due to the higher equivalent potential temperature
 664 and water vapor content of the atmosphere, strong convection persisted in the western
 665 part of the study area in LU_nohgt. The intensity of convection and water droplet
 666 concentration in the atmosphere were markedly higher than those observed in the
 667 LU_2020 scheme. In the zonal direction, significant differences were observed
 668 between the locations of cloud water droplet accumulation between the two
 669 experimental setups. In period T3, convection shifted northward with the southerly
 670 winds in the LU_nohgt scheme. At the southern edge of the convective cloud mass,
 671 the distributions of the wind speed, temperature, and humidity stabilized, indicating
 672 the cessation of intense precipitation in the region. Despite the high energy levels

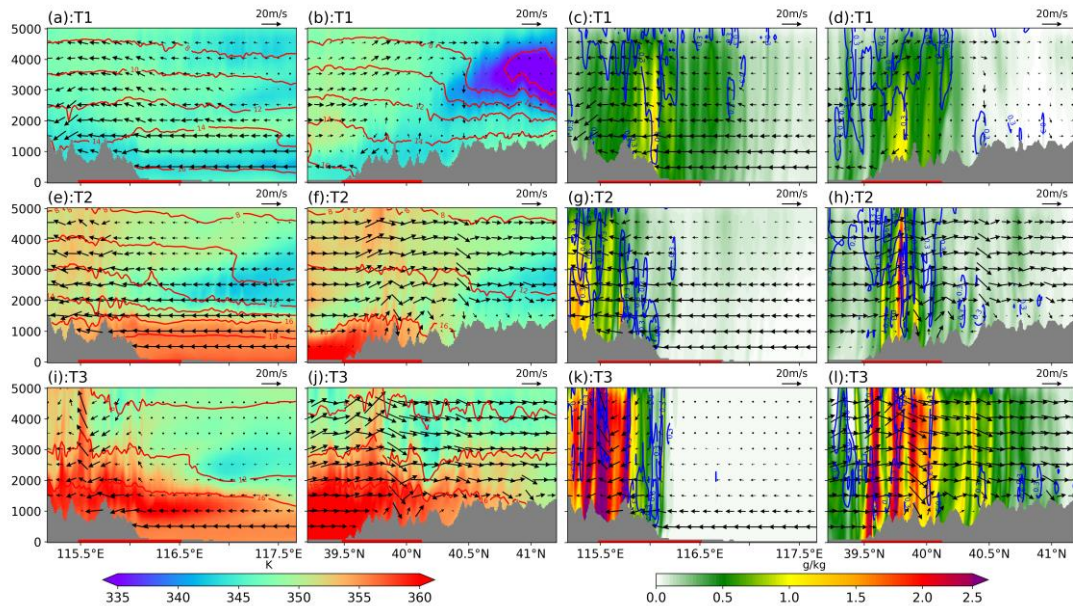
673 within the study area, the absence of orographic uplift led to a reduction in the
 674 intensity of precipitation, and the precipitation event ended earlier compared with the
 675 LU_2020 scheme.



676
 677 **Figure 14:** Meridional-vertical and zonal-vertical profiles for the LU_nohgt schemes. The
 678 physical quantities are consistent with those shown in Figure 12.
 679

680 The impacts of urbanization on precipitation outcomes were examined by
 681 comparing the LU_2020 (Figure 13) and LU_nourb (Figure 15) schemes, where the
 682 primary effects were observed during periods T2 and T3. Due to the influence of
 683 urbanization, there were no significant changes in the cloud water content over the
 684 mountainous areas during period T2, besides the rainwater content was markedly
 685 reduced, indicating a smaller amount of precipitation relative to LU_nourb.
 686 Urbanization led to decreases in the water vapor and energy transported into the
 687 mountains from the eastern and southern parts of the region, thereby reducing the
 688 condensation of cloud water and water vapor particles, which also agreed with the
 689 delayed precipitation during T2 due to urbanization. During period T3, both the
 690 meridional and zonal convection activities were weaker compared with LU_nourb,
 691 and the distribution of cloud droplet particles were also altered. The presence of the
 692 city reduced the latent heat flux in the region, thereby diminishing the amount of
 693 energy transported into the southwestern mountainous areas, and thus intense

694 precipitation occurred in the southwestern mountainous region during periods T2 to
695 T3.



696 **Figure 15:** Meridional-vertical and zonal-vertical profiles for the LU_nourb schemes. The
697 physical quantities are consistent with those shown in Figure 12.
698

699

700 4. Discussion

701 4.1 The intention of experiment design

702 In this study, simulations were conducted using the WRF model to investigate
703 the changes in the timing and spatial distribution of precipitation during the “23 7”
704 event caused by the effects of orography and urban land use. Previous studies have
705 also analyzed the mechanisms related to precipitation and the impacts of orography on
706 extreme precipitation events (Gao et al. 2024; Li et al. 2024b). In contrast to previous
707 analyses, the effects of mountain-plain orographic conditions were explored by
708 altering the underlying surfaces as well as investigating the impact of urbanization on
709 this extreme precipitation event. The primary causes of this extreme precipitation
710 event were identified by considering three time periods with significant differences in
711 precipitation and analyzing the changes in basic physical quantities.

712 It has been pointed out that regional climate models have some limits on
713 reproducing large-scale circulation features (Kukulies et al. 2023; Yu et al. 2024). To
714 address this limitation, spectral nudging to the D01 domain was applied in all schemes.

715 The ERA5 reanalysis data was used to constrain large-scale circulation of the model,
716 while allowing freely development for mesoscale and small-scale processes within the
717 domain (Ma et al. 2022; Miguez-Macho et al. 2005; von Storch et al. 2000; Waldron
718 et al. 1996). Therefore, it can provide a more accurate large-scale flow fields to the
719 inner domains. The simulation results showed that, the orography and land use
720 modifications in this study primarily influenced local circulation patterns and had
721 limited impacts on synoptic-scale weather systems.

722

723 4.2 Comparisons with related studies

724 According to previous research, the maximum reduction in precipitation due to
725 urbanization during warm-season rainfall occurs in the northeastern region of Beijing
726 (Song et al. 2014; Wang et al. 2018). However, in the present study, the largest
727 reduction in precipitation induced by urbanization was observed in the southwestern
728 mountainous region. This difference is mainly caused by the different response
729 patterns of mean and extreme precipitation events. The climatological statistics
730 represent response of mean state, while extreme precipitation is often governed by
731 nonlinear, specific dynamical forcing, and that may cause different distribution pattern
732 (Liu and Niyogi 2019). As shown in the results, the water vapor transport of this
733 precipitation event was mainly dominated by the southeasterly water vapor flux
734 governed by the large-scale circulation, which thus triggered precipitation in the
735 southwestern piedmont area of the Taihang Mountains. Although precipitation also
736 occurred in the northwestern region, its intensity was weaker than that in the
737 southwestern region, which is also the reason why this precipitation event is distinct
738 from others. Therefore, compared with the changes in the average distribution of
739 seasonal precipitation in Beijing found in previous studies, individual case
740 experiments may simulate precipitation distribution patterns that differ from the
741 multi-year observed accumulated precipitation.

742 Previous studies also found that, the modifications of local urban land surface
743 can influence local-scale atmospheric circulation (Kim et al. 2021; Sui et al. 2024;

744 Zajic et al. 2011). The widespread presence of impervious surfaces in urban areas
745 restrained surface evaporation, by reducing the upward transport of moisture into the
746 atmosphere. This process can lead to low relative humidity and reduce atmospheric
747 instability, which in turn modifies the local precipitation distribution (Wang et al.
748 2018). For the extreme precipitation event occurred on July 21 2012, the precipitation
749 event was mostly generated by convective cells that were triggered by local orography
750 and then propagated along a quasi-stationary linear convective system (Zhang et al.
751 2013a). According to analyses of multiple extreme precipitation events in Beijing in
752 recent years, urbanization can reduce rainfall in the urban area and increases rainfall
753 downwind of the city. In some cases, the larger percentage of sealed area could give
754 rise to the heavier precipitation or extreme rain events (Liu et al. 2021). As different
755 types of precipitation or different weather conditions can lead to complex
756 relationships between precipitation and elevation, even along the same slope (Gnann
757 et al. 2025; Houze Jr. 2012). Therefore, urban effects of each event should be
758 analyzed independently (Liu et al. 2021). This precipitation event is somewhat
759 representative; however, for precipitation events under different initial conditions,
760 further investigation is needed.

761

762 4.3 Uncertainty in the experiment simulation

763 The choice of removing the terrain with an elevation above 100 meters was
764 adopted in this study to ensure that the terrain in other regions would not be affected
765 while eliminates the terrain of the Taihang and Yanshan Mountains. Similar
766 experimental design had been used in other researches (Boos and Kuang 2010; Insel
767 et al. 2010; Saurral et al. 2015; Song and Shao 2023). To detect the influence of the
768 terrain removal operation, the experiment was repeated after removing all the terrain
769 in the entire research area and the simulation of completely flat terrain was explored.
770 It can be seen from Figure S5 that the spatial patterns of precipitation are similar for
771 the schemes of 100 m and 0 m removal experiment. The center of maximum
772 precipitation in 0 m removal experiment shifts eastward. This is mainly because the

773 flat terrain enhanced the northward transport of water vapor and further slowed the
774 dissipation of the remnant low of Doksuri. It therefore increases the precipitable water
775 over the region and leads to a more intense precipitation event. Statistically, the mean
776 precipitation intensity is 4.2 mm/hr and 4.7 mm/hr for the 100 m and 0 m removal
777 experiment, respectively. The RMSE and MAE of precipitation intensity is 1.54
778 mm/hr and 1.17 mm/hr between these two schemes and the correlation coefficient is
779 0.74. The results proved the strong relationships between the precipitations from 100
780 m and 0 m removal experiment schemes, which may apply to other precipitation
781 related variables.

782 The simulations were conducted using selected parameterization schemes and
783 the impacts of the underlying surface were analyzed in this study. Physical
784 parameterization schemes are widely recognized to exert substantial impacts on
785 precipitation simulations, affecting not only intensity and duration, but also
786 spatiotemporal distribution patterns. The parameterization method adopted in this
787 study had also been used in other studies about urban extreme precipitation events
788 (Luo et al. 2023; Ryu et al. 2016; Wang et al. 2018; Wang et al. 2023; Xian et al.
789 2023), which can partly can prove the rationality of this study. Additional
790 investigations into the parameterization schemes governing this precipitation event
791 are required to elucidate the specific atmospheric conditions and physical mechanisms.
792 Furthermore, due to constraints in data accessibility, only the 2020 MODIS land use
793 dataset was obtained and used in our simulations, despite potential temporal
794 mismatches with other input data periods. The Sentinel-2 satellite observations were
795 further detected to assess the potential biases in land use between 2020 and 2023. The
796 urban extent exhibited minimal variation between these years (Figure S6), validating
797 the temporal stability of the MODIS baseline. However, the inherent differences in
798 classification schemes between MODIS and Sentinel-2 precluded direct data
799 integration or substitution. Therefore, the 2020 MODIS dataset was retained as the
800 most recent consistent one, though it may introduce some uncertainties into the results.

801 Besides, the concentrations of aerosols emitted in urban areas could also have

802 influenced the extreme precipitation because it is largely driven by the coalescence of
803 cloud droplets. Studies have shown that aerosols can lead to the formation of smaller-
804 sized cloud droplets, increasing the effective radius of precipitation, and thus impact
805 convective rainfall (Sun et al. 2022; Zhong et al. 2015). In addition, topographic
806 variations can also affect the generation of cloud particles (Lee et al. 2018; Mazzetti et
807 al. 2021). However, this study focuses on the impact of natural factors, particularly
808 the underlying surface, on precipitation events. Aerosols are largely attributed to
809 anthropogenic factors, therefore are not involved in this study and would be
810 considered in future research.

811

812 **5. Conclusion**

813 In this study, the WRF model was used to analyze the extreme precipitation
814 event that occurred in the Beijing region from July 29 to August 2, 2023. The effects
815 of orography and land use on the precipitation process were evaluated by removing
816 the orography and replacing urban land use types with croplands from the updated
817 land use experiment group. The results showed that, the areas influenced most
818 significantly by orography were concentrated in the southwestern mountainous region
819 of Beijing. Presence of terrain caused orographic uplift and increased the precipitation
820 within the mountainous area by more than 40% during the event. This main because
821 that the mountainous area blocked the existence of the low-pressure system of
822 typhoon Doksuri from propagating northward and lead to extended duration of the
823 precipitation event by approximately 12 h. The underlying urban surfaces also altered
824 the overall precipitation process. For the scheme removing the underlying urban
825 surfaces the enhanced water vapor flux transported by low-level easterly winds to the
826 southwestern mountainous region of the city increased the accumulation of energy
827 and water vapor in the region. After July 31, the accumulation of sufficient energy and
828 moisture in the southwestern mountainous region strengthened the intensity of
829 precipitation. In addition, removing the underlying urban surface caused an increase
830 in the wind speed in the plain areas, which led to large convergence at the mountain

831 boundary and contributed to stronger precipitation. These findings can help us with
832 the prevention and response to similar future events, and possibly reduce the
833 likelihood of disasters.

834

835 **Financial Support**

836 This study was funded by the National Natural Science Foundation of China
837 (42077421 and 41930970).

838

839 **Data Availability Statement**

840 The ERA5 reanalysis data can be downloaded at Climate Data Store
841 (<https://cds.climate.copernicus.eu>). The gauge observations were from the China
842 Meteorological Administration (version 2.0; <http://data.cma.cn/en>). The CMOPRH
843 precipitation data were obtained from Climate Prediction Center.
844 (<https://www.ncei.noaa.gov/products/climate-data-records/precipitation-cmorph>). The
845 updated land use/land cover data from MCD12Q1 V6 over Beijing region are
846 available from the Land Processes Distributed Active Archive Center
847 (<https://lpdaac.usgs.gov/>).

848

849 **Author Contributions**

850 **HC**: Conceptualization; formal analysis; methodology; software; validation;
851 visualization; writing – original draft; writing – review and editing. **HY**:
852 Conceptualization; methodology; writing – review and editing. **XZ**: methodology;
853 writing – review and editing. **GW**: Conceptualization; data curation; funding
854 acquisition; investigation resources; supervision; writing – original draft; writing –
855 review and editing.

856

857 **Conflicts of Interest**

858 The authors declare that they have no conflict of interest.

859

860 **References**

- 861 Ayat, H., J. P. Evans, S. C. Sherwood, and J. Soderholm, 2022: Intensification of subhourly heavy
862 rainfall. *Science*, 378, 655-+.
- 863 Bhattarai, S., and R. Talchabhadel, 2024: Comparative Analysis of Satellite -Based Precipitation
864 Data across the CONUS and Hawaii: Identifying Optimal Satellite Performance. *Remote*
865 *Sensing*, 16, 3058.
- 866 Boos, W. R., and Z. Kuang, 2010: Dominant control of the South Asian monsoon by orographic
867 insulation versus plateau heating. *Nature*, 463, 218-222.
- 868 Bornstein, R., and Q. L. Lin, 2000: Urban heat islands and summertime convective thunderstorms
869 in Atlanta: three case studies. *Atmospheric Environment*, 34, 507-516.
- 870 Chen, F., and J. Dudhia, 2001: Coupling an advanced land surface-hydrology model with the
871 Penn State-NCAR MM5 modeling system. Part II: Preliminary model validation. *Monthly*
872 *Weather Review*, 129, 587-604.
- 873 Chen, F., H. Kusaka, R. Bornstein, J. Ching, C. S. B. Grimmond, S. Grossman-Clarke, T. Loridan, K.
874 W. Manning, A. Martilli, S. G. Miao, D. Sailor, F. P. Salamanca, H. Taha, M. Tewari, X. M.
875 Wang, A. A. Wyszogrodzki, and C. L. Zhang, 2011: The integrated WRF/urban modelling
876 system: development, evaluation, and applications to urban environmental problems.
877 *International Journal of Climatology*, 31, 273-288.
- 878 Chen, M. X., Y. C. Wang, F. Gao, and X. Xiao, 2014: Diurnal evolution and distribution of warm-
879 season convective storms in different prevailing wind regimes over contiguous North
880 China. *Journal of Geophysical Research-Atmospheres*, 119, 2742-2763.
- 881 Cornejo, I. C., A. K. Rowel, K. L. Rasmussen, and J. C. Dehartb, 2024: Orographic Controls on
882 Extreme Precipitation Associated with a Mei-Yu Front. *Monthly Weather Review*, 152,
883 531-551.
- 884 Dai, P. X., J. Nie, Y. Yu, and R. G. Wu, 2024: Constraints on regional projections of mean and
885 extreme precipitation under warming. *Proceedings of the National Academy of Sciences*
886 *of the United States of America*, 121.
- 887 Davolio, S., A. Buzzi, and P. Malguzzi, 2009: Orographic triggering of long lived convection in
888 three dimensions. *Meteorology and Atmospheric Physics*, 103, 35-44.
- 889 Dixon, P. G., and T. L. Mote, 2003: Patterns and causes of Atlanta's urban heat island-initiated
890 precipitation. *Journal of Applied Meteorology*, 42, 1273-1284.
- 891 Dou, J. J., Y. C. Wang, R. Bornstein, and S. G. Miao, 2015: Observed Spatial Characteristics of
892 Beijing Urban Climate Impacts on Summer Thunderstorms. *Journal of Applied*
893 *Meteorology and Climatology*, 54, 94-105.
- 894 Du, Y., G. X. Chen, B. Han, L. Q. Bai, and M. H. Li, 2020: Convection Initiation and Growth at the
895 Coast of South China. Part II: Effects of the Terrain, Coastline, and Cold Pools. *Monthly*
896 *Weather Review*, 148, 3871-3892.
- 897 Dudhia, J., 1989: Numerical Study of Convection Observed during the Winter Monsoon
898 Experiment Using a Mesoscale Two-Dimensional Model. *Journal of the Atmospheric*
899 *Sciences*, 46, 3077-3107.
- 900 Ebert, E. E., J. E. Janowiak, and C. Kidd, 2007: Comparison of near-real-time precipitation
901 estimates from satellite observations and numerical models. *Bulletin of the American*
902 *Meteorological Society*, 88, 47-64.
- 903 Freitag, B. M., U. S. Nair, and D. Niyogi, 2018: Urban Modification of Convection and Rainfall in

904 Complex Terrain. *Geophysical Research Letters*, 45, 2507-2515.

905 Friedl, M., D. Sulla-Menashe, 2019: MCD12Q1 MODIS/Terra+Aqua Land Cover Type Yearly L3
906 Global 500m SIN Grid V006. NASA EOSDIS Land Processes Distributed Active Archive
907 Center.

908 Fu, Y. Y., S. J. Jiang, Y. N. Mao, and G. C. Wu, 2024: Urbanization reshapes extreme precipitation
909 metrics in typical urban agglomerations of Eastern China. *Atmospheric Research*, 300.

910 Gao, X. Y., J. S. Sun, J. F. Yin, A. Abulikemu, C. Wu, X. D. Liang, and R. D. Xia, 2024: The impact of
911 mountain-plain thermal contrast on precipitation distributions during the "23.7" record-
912 breaking heavy rainfall over North China. *Atmospheric Research*, 310.

913 Gao, Z. B., J. S. Zhu, Y. Guo, N. Luo, Y. Fu, and T. T. Wang, 2021: Impact of Land Surface
914 Processes on a Record-Breaking Rainfall Event on May 06-07, 2017, in Guangzhou,
915 China. *Journal of Geophysical Research-Atmospheres*, 126.

916 Gimeno, L., A. Drumond, R. Nieto, R. M. Trigo, and A. Stohl, 2010: On the origin of continental
917 precipitation. *Geophysical Research Letters*, 37.

918 Gnann, S., J. W. Baldwin, M. O. Cuthbert, T. Gleeson, W. Schwanghart, and T. Wagener, 2025: The
919 Influence of Topography on the Global Terrestrial Water Cycle. *Reviews of Geophysics*,
920 63, e2023RG000810.

921 Gómez, B., and G. Miguez-Macho, 2017: The impact of wave number selection and spin-up time
922 in spectral nudging. *Quarterly Journal of the Royal Meteorological Society*, 143, 1772-
923 1786.

924 He, H. Z., and F. Q. Zhang, 2010: Diurnal Variations of Warm-Season Precipitation over Northern
925 China. *Monthly Weather Review*, 138, 1017-1025.

926 He, Y., J. Wang, and J. Feng, 2023: A Typical Weakly Forced Mountain-To-Plain Extreme
927 Precipitation Event Exacerbated by Urbanization in Beijing. *Journal of Geophysical
928 Research: Atmospheres*, 128, e2023JD039275.

929 Hersbach, H., B. Bell, P. Berrisford, S. Hirahara, A. Horányi, J. Muñoz-Sabater, J. Nicolas, C.
930 Peubey, R. Radu, D. Schepers, A. Simmons, C. Soci, S. Abdalla, X. Abellan, G. Balsamo, P.
931 Bechtold, G. Biavati, J. Bidlot, M. Bonavita, G. De Chiara, P. Dahlgren, D. Dee, M.
932 Diamantakis, R. Dragani, J. Flemming, R. Forbes, M. Fuentes, A. Geer, L. Haimberger, S.
933 Healy, R. J. Hogan, E. Hólm, M. Janisková, S. Keeley, P. Laloyaux, P. Lopez, C. Lupu, G.
934 Radnoti, P. de Rosnay, I. Rozum, F. Vamborg, S. Villaume, and J.-N. Thépaut, 2020a: The
935 ERA5 global reanalysis. *Quarterly Journal of the Royal Meteorological Society*, 146,
936 1999-2049.

937 Hersbach, H., B. Bell, P. Berrisford, S. Hirahara, A. Horányi, J. Muñoz-Sabater, J. Nicolas, C.
938 Peubey, R. Radu, D. Schepers, A. Simmons, C. Soci, S. Abdalla, X. Abellan, G. Balsamo, P.
939 Bechtold, G. Biavati, J. Bidlot, M. Bonavita, G. De Chiara, P. Dahlgren, D. Dee, M.
940 Diamantakis, R. Dragani, J. Flemming, R. Forbes, M. Fuentes, A. Geer, L. Haimberger, S.
941 Healy, R. J. Hogan, E. Hólm, M. Janisková, S. Keeley, P. Laloyaux, P. Lopez, C. Lupu, G.
942 Radnoti, P. de Rosnay, I. Rozum, F. Vamborg, S. Villaume, and J. N. Thépaut, 2020b: The
943 ERA5 global reanalysis. *Quarterly Journal of the Royal Meteorological Society*, 146,
944 1999-2049.

945 Hjelmfelt, M. R., 1982: Numerical Simulation of the Effects of St. Louis on Mesoscale Boundary-
946 Layer Airflow and Vertical Air Motion: Simulations of Urban vs Non-Urban Effects.
947 *Journal of Applied Meteorology*, 21, 1239-1257.

948 Holst, C. C., C.-Y. Tam, and J. C. L. Chan, 2016: Sensitivity of urban rainfall to anthropogenic heat
949 flux: A numerical experiment. *Geophysical Research Letters*, 43, 2240-2248.

950 Hong, S. Y., Y. Noh, and J. Dudhia, 2006: A new vertical diffusion package with an explicit
951 treatment of entrainment processes. *Monthly Weather Review*, 134, 2318-2341.

952 Hong, S. Y., and J.-O. J. Lim, 2006: The WRF single-moment 6-class microphysics scheme
953 (WSM6). *Journal of the Korean Meteorological Society*, 42, 129-151.

954 Houze Jr., R. A., 2012: Orographic effects on precipitating clouds. *Reviews of Geophysics*, 50.

955 Huang, Y. J., Y. B. Liu, Y. W. Liu, H. Y. Li, and J. C. Kniviel, 2019: Mechanisms for a Record-
956 Breaking Rainfall in the Coastal Metropolitan City of Guangzhou, China: Observation
957 Analysis and Nested Very Large Eddy Simulation With the WRF Model. *Journal of*
958 *Geophysical Research-Atmospheres*, 124, 1370-1391.

959 Insel, N., C. J. Poulsen, and T. A. Ehlers, 2010: Influence of the Andes Mountains on South
960 American moisture transport, convection, and precipitation. *Climate Dynamics*, 35,
961 1477-1492.

962 Janjić, Z. I., 1994: The Step-Mountain Eta Coordinate Model: Further Developments of the
963 Convection, Viscous Sublayer, and Turbulence Closure Schemes. *Monthly Weather*
964 *Review*, 122, 927-945.

965 Jauregui, E., and E. Romales, 1996: Urban effects on convective precipitation in Mexico city.
966 *Atmospheric Environment*, 30, 3383-3389.

967 Jiang, S.-h., M. Zhou, L.-l. Ren, X.-r. Cheng, and P.-j. Zhang, 2016: Evaluation of latest TMPA and
968 CMORPH satellite precipitation products over Yellow River Basin. *Water Science and*
969 *Engineering*, 9, 87-96.

970 Joyce, R. J., J. E. Janowiak, P. A. Arkin, and P. P. Xie, 2004: CMORPH: A method that produces
971 global precipitation estimates from passive microwave and infrared data at high spatial
972 and temporal resolution. *Journal of Hydrometeorology*, 5, 487-503.

973 Kain, J. S., 2004: The Kain-Fritsch convective parameterization: An update. *Journal of Applied*
974 *Meteorology*, 43, 170-181.

975 Kim, G., J. Lee, M.-l. Lee, and D. Kim, 2021: Impacts of urbanization on atmospheric circulation
976 and aerosol transport in a coastal environment simulated by the WRF-Chem coupled
977 with urban canopy model. *Atmospheric Environment*, 249, 118253.

978 Kukulies, J., A. F. Prein, J. Curio, H. Yu, and D. Chen, 2023: Kilometer-Scale Multimodel and
979 Multiphysics Ensemble Simulations of a Mesoscale Convective System in the Lee of the
980 Tibetan Plateau: Implications for Climate Simulations. *Journal of Climate*, 36, 5963-5987.

981 Lee, J. T., K. Y. Ko, D. I. Lee, C. H. You, and Y. C. Liou, 2018: Enhancement of orographic
982 precipitation in Jeju Island during the passage of Typhoon Khanun (2012). *Atmospheric*
983 *Research*, 201, 58-71.

984 Li, S., Y. N. Chen, W. Wei, G. H. Fang, and W. L. Duan, 2024a: The increase in extreme
985 precipitation and its proportion over global land. *Journal of Hydrology*, 628.

986 Li, W. B., S. Chen, G. X. Chen, W. M. Sha, C. Luo, Y. R. Feng, Z. P. Wen, and B. M. Wang, 2011:
987 Urbanization signatures in strong versus weak precipitation over the Pearl River Delta
988 metropolitan regions of China. *Environmental Research Letters*, 6.

989 Li, X., S. Zhao, and D. Wang, 2024b: Roles of synoptic characteristics and microphysics processes
990 on the heavy rain event over Beijing region during 29 July to 2 August 2023. *Frontiers in*
991 *Earth Science*, Volume 12 - 2024.

992 Li, X., S. W. Zhao, and D. H. Wang, 2024c: Roles of synoptic characteristics and microphysics
993 processes on the heavy rain event over Beijing region during 29 July to 2 August 2023.
994 *Frontiers in Earth Science*, 12.

995 Liang, P., and Y. H. Ding, 2017: The Long-term Variation of Extreme Heavy Precipitation and Its
996 Link to Urbanization Effects in Shanghai during 1916-2014. *Advances in Atmospheric*
997 *Sciences*, 34, 321-334.

998 Lin, Y. L., S. Chiao, T. A. Wang, M. L. Kaplan, and R. P. Weglarz, 2001: Some common ingredients
999 for heavy orographic rainfall. *Weather and Forecasting*, 16, 633-660.

1000 Liu, J., and D. Niyogi, 2019: Meta-analysis of urbanization impact on rainfall modification.
1001 *Scientific Reports*, 9, 7301.

1002 Liu, J., K. H. Schlünzen, T. Frisius, and Z. Tian, 2021: Effects of urbanization on precipitation in
1003 Beijing. *Physics and Chemistry of the Earth, Parts A/B/C*, 122, 103005.

1004 Liu, P., A. P. Tsimpidi, Y. Hu, B. Stone, A. G. Russell, and A. Nenes, 2012: Differences between
1005 downscaling with spectral and grid nudging using WRF. *Atmos. Chem. Phys.*, 12, 3601-
1006 3610.

1007 Liu, S., J. Wang, and H. Wang, 2022: Assessing 10 Satellite Precipitation Products in Capturing the
1008 July 2021 Extreme Heavy Rain in Henan, China. *Journal of Meteorological Research*, 36,
1009 798-808.

1010 Luo, Y., J. Zhang, M. Yu, X. Liang, R. Xia, Y. Gao, X. Gao, and J. Yin, 2023: On the Influences of
1011 Urbanization on the Extreme Rainfall over Zhengzhou on 20 July 2021: A Convection-
1012 Permitting Ensemble Modeling Study. *Advances in Atmospheric Sciences*, 40, 393-409.

1013 Ma, M., P. Hui, D. Liu, P. Zhou, and J. Tang, 2022: Convection-permitting regional climate
1014 simulations over Tibetan Plateau: re-initialization versus spectral nudging. *Climate*
1015 *Dynamics*, 58, 1719-1735.

1016 Ma, Y., Y. Yang, X. Mai, C. Qiu, X. Long, and C. Wang, 2016: Comparison of Analysis and Spectral
1017 Nudging Techniques for Dynamical Downscaling with the WRF Model over China.
1018 *Advances in Meteorology*, 2016, 4761513.

1019 Mahoney, K. M., 2016: The Representation of Cumulus Convection in High-Resolution
1020 Simulations of the 2013 Colorado Front Range Flood. *Monthly Weather Review*, 144,
1021 4265-4278.

1022 Mazzetti, T. O., B. Geerts, L. L. Xue, S. Tessorf, C. Weeks, and Y. G. Wang, 2021: Potential for
1023 Ground-Based Glaciogenic Cloud Seeding over Mountains in the Interior Western
1024 United States and Anticipated Changes in a Warmer Climate. *Journal of Applied*
1025 *Meteorology and Climatology*, 60, 1245-1263.

1026 Miguez-Macho, G., G. L. Stenchikov, and A. Robock, 2004: Spectral nudging to eliminate the
1027 effects of domain position and geometry in regional climate model simulations. *Journal*
1028 *of Geophysical Research-Atmospheres*, 109.

1029 Miguez-Macho, G., G. L. Stenchikov, and A. Robock, 2005: Regional Climate Simulations over
1030 North America: Interaction of Local Processes with Improved Large-Scale Flow. *Journal*
1031 *of Climate*, 18, 1227-1246.

1032 Mlawer, E. J., S. J. Taubman, P. D. Brown, M. J. Iacono, and S. A. Clough, 1997: Radiative transfer
1033 for inhomogeneous atmospheres: RRTM, a validated correlated-k model for the
1034 longwave. *Journal of Geophysical Research-Atmospheres*, 102, 16663-16682.

1035 Nicolas, Q., and W. R. Boos, 2024: Understanding the Spatiotemporal Variability of Tropical

1036 Orographic Rainfall Using Convective Plume Buoyancy. *Journal of Climate*, 37, 1737-
1037 1757.

1038 Nie, W. S., B. F. Zaitchik, G. H. Ni, and T. Sun, 2017: Impacts of Anthropogenic Heat on
1039 Summertime Rainfall in Beijing. *Journal of Hydrometeorology*, 18, 693-712.

1040 Niyogi, D., P. Pyle, M. Lei, S. P. Arya, C. M. Kishtawal, M. Shepherd, F. Chen, and B. Wolfe, 2011:
1041 Urban Modification of Thunderstorms: An Observational Storm Climatology and Model
1042 Case Study for the Indianapolis Urban Region. *Journal of Applied Meteorology and
1043 Climatology*, 50, 1129-1144.

1044 Oke, T. R., 1982: The energetic basis of the urban heat island. *Quarterly Journal of the Royal
1045 Meteorological Society*, 108, 1-24.

1046 Pei, L., S.-G. Miao, X.-Y. Huang, Z.-W. Yan, and D. Chen, 2025: Assessing the added value of
1047 convection-permitting modeling for urban climate research: A case study in eastern
1048 China. *Advances in Climate Change Research*, 16, 1-11.

1049 Pendergrass, A. G., and R. Knutti, 2018: The Uneven Nature of Daily Precipitation and Its Change.
1050 *Geophysical Research Letters*, 45, 11980-11988.

1051 Ryu, Y.-H., J. A. Smith, E. Bou-Zeid, and M. L. Baeck, 2016: The Influence of Land Surface
1052 Heterogeneities on Heavy Convective Rainfall in the Baltimore–Washington
1053 Metropolitan Area. *Monthly Weather Review*, 144, 553-573.

1054 Saurral, R. I., I. A. Camilloni, and T. Ambrizzi, 2015: Links between topography, moisture fluxes
1055 pathways and precipitation over South America. *Climate Dynamics*, 45, 777-789.

1056 Skamarock, W. C., J. B. Klemp, J. Dudhia, D. O. Gill, Z. Liu, J. Berner, W. Wang, J. G. Powers, M. G.
1057 Duda, D. M. Barker, and X.-Y. Huang, 2019: A Description of the Advanced Research
1058 WRF Version 4. NCAR Tech. Note NCAR/TN-556+STR, 145 pp.

1059 Smith, R. B., 2006: Progress on the theory of orographic precipitation. *Tectonics, Climate, and
1060 Landscape Evolution*, 1-16.

1061 Song, X. M., J. Y. Zhang, A. AghaKouchak, S. Sen Roy, Y. Q. Xuan, G. Q. Wang, R. M. He, X. J.
1062 Wang, and C. S. Liu, 2014: Rapid urbanization and changes in spatiotemporal
1063 characteristics of precipitation in Beijing metropolitan area. *Journal of Geophysical
1064 Research-Atmospheres*, 119, 11250-11271.

1065 Song, Y., and M. Shao, 2023: Impacts of Complex Terrain Features on Local Wind Field and
1066 PM_{2.5} Concentration. *Atmosphere*, 761.

1067 Spero, T. L., M. J. Otte, J. H. Bowden, and C. G. Nolte, 2014: Improving the representation of
1068 clouds, radiation, and precipitation using spectral nudging in the Weather Research and
1069 Forecasting model. *Journal of Geophysical Research-Atmospheres*, 119, 11682-11694.

1070 Sui, X., Z.-L. Yang, M. Shepherd, and D. Niyogi, 2024: Global scale assessment of urban
1071 precipitation anomalies. *Proceedings of the National Academy of Sciences*, 121,
1072 e2311496121.

1073 Sun, N., Y. F. Fu, L. Zhong, and R. Li, 2022: Aerosol effects on the vertical structure of
1074 precipitation in East China. *NPJ Climate and Atmospheric Science*, 5.

1075 Sun, Q., X. Zhang, F. Zwiers, S. Westra, and L. V. Alexander, 2021: A Global, Continental, and
1076 Regional Analysis of Changes in Extreme Precipitation. *Journal of Climate*, 34, 243-258.

1077 Sun, R., H. Yuan, X. Liu, and X. Jiang, 2016: Evaluation of the latest satellite–gauge precipitation
1078 products and their hydrologic applications over the Huaihe River basin. *Journal of
1079 Hydrology*, 536, 302-319.

1080 Tewari, M., F. Chen, J. Dudhia, P. Ray, S. G. Miao, E. Nikolopoulos, and L. Treinish, 2022:
1081 Understanding the sensitivity of WRF hindcast of Beijing extreme rainfall of 21 July 2012
1082 to microphysics and model initial time. *Atmospheric Research*, 271.

1083 Trenberth, K. E., A. Dai, R. M. Rasmussen, and D. B. Parsons, 2003: The changing character of
1084 precipitation. *Bulletin of the American Meteorological Society*, 84, 1205-1217.

1085 von Storch, H., H. Langenberg, and F. Feser, 2000: A spectral nudging technique for dynamical
1086 downscaling purposes. *Monthly Weather Review*, 128, 3664-3673.

1087 Waldron, K. M., J. Paegle, and J. D. Horel, 1996: Sensitivity of a Spectrally Filtered and Nudged
1088 Limited-Area Model to Outer Model Options. *Monthly Weather Review*, 124, 529-547.

1089 Wang, J., J. M. Feng, and Z. W. Yan, 2015: Potential sensitivity of warm season precipitation to
1090 urbanization extents: Modeling study in Beijing-Tianjin-Hebei urban agglomeration in
1091 China. *Journal of Geophysical Research-Atmospheres*, 120, 9408-9425.

1092 Wang, J., J. Feng, and Z. Yan, 2018: Impact of Extensive Urbanization on Summertime Rainfall in
1093 the Beijing Region and the Role of Local Precipitation Recycling. *Journal of Geophysical
1094 Research: Atmospheres*, 123, 3323-3340.

1095 Wang, J., S. Miao, Q.-V. Doan, F. Chen, R. Abolafia-Rosenzweig, L. Yang, G. Zhang, Y. Zhang, J.
1096 Dou, and Y. Xu, 2023: Quantifying the Impacts of High-Resolution Urban Information on
1097 the Urban Thermal Environment. *Journal of Geophysical Research: Atmospheres*, 128,
1098 e2022JD038048.

1099 Wang, X. Q., and Y. B. Gong, 2010: The impact of an urban dry island on the summer heat wave
1100 and sultry weather in Beijing City. *Chinese Science Bulletin*, 55, 1657-1661.

1101 Wei, P., X. Xu, M. Xue, C. Y. Zhang, Y. Wang, K. Zhao, A. Zhou, S. S. Zhang, and K. F. Zhu, 2023:
1102 On the Key Dynamical Processes Supporting the 21.7 Zhengzhou Record-breaking
1103 Hourly Rainfall in China. *Advances in Atmospheric Sciences*, 40, 337-349.

1104 Wu, G. C., Y. Li, S. Qin, Y. N. Mao, and K. C. Wang, 2021: Precipitation Unevenness in Gauge
1105 Observations and Eight Reanalyses from 1979 to 2018 over China. *Journal of Climate*, 34,
1106 9797-9810.

1107 Xia, R. D., and D. L. Zhang, 2019: An Observational Analysis of Three Extreme Rainfall Episodes of
1108 19-20 July 2016 along the Taihang Mountains in North China. *Monthly Weather Review*,
1109 147, 4199-4220.

1110 Xian, T., J. Guo, R. Zhao, T. Su, and Z. Li, 2023: The Impact of Urbanization on Mesoscale
1111 Convective Systems in the Yangtze River Delta Region of China: Insights Gained From
1112 Observations and Modeling. *Journal of Geophysical Research: Atmospheres*, 128,
1113 e2022JD037709.

1114 Yang, P., G. Y. Ren, and P. C. Yan, 2017: Evidence for a Strong Association of Short-Duration
1115 Intense Rainfall with Urbanization in the Beijing Urban Area. *Journal of Climate*, 30,
1116 5851-5870.

1117 Yin, J. F., D. L. Zhang, Y. L. Luo, and R. Y. Ma, 2020: On the Extreme Rainfall Event of 7 May 2017
1118 over the Coastal City of Guangzhou. Part I: Impacts of Urbanization and Orography.
1119 *Monthly Weather Review*, 148, 955-979.

1120 Yu, H., A. F. Prein, D. Qi, and K. Wang, 2024: Kilometer-scale multi-physics simulations of heavy
1121 precipitation events in Northeast China. *Climate Dynamics*, 62, 9207-9231.

1122 Yu, M., and Y. M. Liu, 2015: The possible impact of urbanization on a heavy rainfall event in
1123 Beijing. *Journal of Geophysical Research-Atmospheres*, 120, 8132-8143.

1124 Yu, M., S. G. Miao, and Q. C. Li, 2017: Synoptic analysis and urban signatures of a heavy rainfall
1125 on 7 August 2015 in Beijing. *Journal of Geophysical Research-Atmospheres*, 122, 65-78.
1126 Zajic, D., H. J. S. Fernando, R. Calhoun, M. Princevac, M. J. Brown, and E. R. Pardyjak, 2011: Flow
1127 and Turbulence in an Urban Canyon. *Journal of Applied Meteorology and Climatology*,
1128 50, 203-223.
1129 Zhang, D.-L., Y. Lin, P. Zhao, X. Yu, S. Wang, H. Kang, and Y. Ding, 2013a: The Beijing extreme
1130 rainfall of 21 July 2012: "Right results" but for wrong reasons. *Geophysical Research*
1131 *Letters*, 40, 1426-1431.
1132 Zhang, D. L., Y. H. Lin, P. Zhao, X. D. Yu, S. Q. Wang, H. W. Kang, and Y. H. Ding, 2013b: The
1133 Beijing extreme rainfall of 21 July 2012: "Right results" but for wrong reasons.
1134 *Geophysical Research Letters*, 40.
1135 Zhang, W. X., K. Furtado, T. J. Zhou, P. L. Wu, and X. L. Chen, 2022: Constraining extreme
1136 precipitation projections using past precipitation variability. *Nature Communications*, 13.
1137 Zhang, Y. Z., S. G. Miao, Y. J. Dai, and R. Bornstein, 2017: Numerical simulation of urban land
1138 surface effects on summer convective rainfall under different UHI intensity in Beijing.
1139 *Journal of Geophysical Research-Atmospheres*, 122, 7851-7868.
1140 Zhong, S., Y. Qian, C. Zhao, R. Leung, and X. Q. Yang, 2015: A case study of urbanization impact
1141 on summer precipitation in the Greater Beijing Metropolitan Area: Urban heat island
1142 versus aerosol effects. *Journal of Geophysical Research-Atmospheres*, 120, 10903-
1143 10914.
1144